

# Biomimetic piezoelectric nanomaterial-modified oral microrobots for targeted catalytic and immunotherapy of colorectal cancer

Yueyue Fan<sup>1†</sup>, Jiamin Ye<sup>1†</sup>, Yong Kang<sup>1†</sup>, Gaoli Niu<sup>1</sup>, Jiacheng Shi<sup>1</sup>, Xue Yuan<sup>1</sup>, Ruiyan Li<sup>1</sup>, Jingwen Han<sup>1</sup>, Xiaoyuan Ji<sup>1,2\*</sup>

Lactic acid (LA) accumulation in the tumor microenvironment poses notable challenges to effective tumor immunotherapy. Here, an intelligent tumor treatment microrobot based on the unique physiological structure and metabolic characteristics of *Veillonella atypica* (VA) is proposed by loading *Staphylococcus aureus* cell membrane-coating BaTiO<sub>3</sub> nanocubes (SAM@BTO) on the surface of VA cells (VA-SAM@BTO) via click chemical reaction. Following oral administration, VA-SAM@BTO accurately targeted orthotopic colorectal cancer through inflammatory targeting of SAM and hypoxic targeting of VA. Under in vitro ultrasonic stimulation, BTO catalyzed two reduction reactions ( $O_2 \rightarrow O_2^-$  and  $CO_2 \rightarrow CO$ ) and three oxidation reactions ( $H_2O \rightarrow OH$ , GSH  $\rightarrow$  GSSG, and LA  $\rightarrow$  PA) simultaneously, effectively inducing immunogenic death of tumor cells. BTO catalyzed the oxidative coupling of VA cells metabolized LA, effectively disrupting the immunosuppressive microenvironment, improving dendritic cell maturation and macrophage M1 polarization, and increasing effector T cell proportions while decreasing regulatory T cell numbers, which facilitates synergetic catalysis and immunotherapy.

Copyright © 2024 The Authors, some rights reserved; exclusive licensee American Association for the Advancement of Science. No claim to original U.S. Government Works. Distributed under a Creative Commons Attribution NonCommercial License 4.0 (CC BY-NC).

## INTRODUCTION

Tumor immunotherapy has emerged as a promising approach to cancer treatment, harnessing the body's immune system to target and eliminate cancer cells. However, the tumor microenvironment (TME) presents numerous challenges that can impede the effectiveness of immunotherapeutic interventions (1, 2). One crucial factor in the TME is the accumulation of lactic acid (LA), which is a metabolic byproduct of increased glycolysis in cancer cells (3, 4). LA has been identified as a key player in shaping the TME and influencing the response to immunotherapy (5). The impact of LA on tumor immunotherapy is multifaceted and encompasses various aspects of immune cell function and tumor progression (6). It has been observed that LA affects the proliferation, activation, and cytotoxicity of immune cells involved in tumor defense, such as T cells, macrophages, and dendritic cells (DCs) (7, 8). The inhibitory effects of LA on these immune cells compromise their ability to effectively recognize and eliminate cancer cells, thus limiting the therapeutic potential of immunotherapy (9). Furthermore, LA promotes the differentiation of immune cells into regulatory T cells (T<sub>regs</sub>) within the TME (10). T<sub>regs</sub> play a critical role in immune tolerance and suppression of antitumor immune responses, allowing cancer cells to evade the immune system and propagate (11, 12). This further highlights the detrimental effect of LA on tumor immunotherapy. In addition to its impact on immune cells, LA also contributes to tumor progression (13). It stimulates angiogenesis, the formation of new blood vessels, which is crucial for providing nutrients and oxygen to growing tumors (14). Moreover, LA facilitates extracellular matrix remodeling, which promotes tumor invasion and metastasis (2, 15).

Understanding the influence of LA on tumor immunotherapy is vital for developing strategies to overcome its inhibitory effects (16, 17). Efforts have been made to neutralize the acidic pH of the TME and reduce LA accumulation using alkaline buffers, proton pump inhibitors, and lactate oxidase (18). Recent advances in microbiology and immunology have facilitated the development of innovative approaches for microbiology-based tumor therapy (19–21). The use of oncolytic viruses, which selectively replicate and destroy cancer cells while sparing normal cells, has shown promising results in pre-clinical and clinical studies (22–24). Oncolytic viruses can be engineered to enhance their therapeutic potential and improve their specificity toward cancer cells (25). Another approach in microbiology-based tumor therapy involves the use of bacterial strains that have been genetically modified to produce therapeutic proteins or toxins that target cancer cells (26, 27). These bacteria can be used as vehicles to deliver drugs directly to the tumor site, reducing systemic toxicity and improving treatment efficacy (26, 28). In addition, some bacteria have intrinsic immunostimulatory properties that can enhance the antitumor immune response (29, 30).

*Veillonella atypica* (VA) is a kind of beneficial microorganism widely found in the human body, mainly distributed in the mouth, respiratory tract, and digestive tract. Its main function is to degrade acidic substances produced by other microorganisms or cells (31). In a study published in 2015 by the Joslin Diabetes Center and the Kostic Laboratory at Harvard Medical School (31), it was found that the VA uses LA as a food source and produces propionate. As a result of this finding, the VA has been referred to as a "performance-enhancing microbe." Considering the impact of LA on tumor immune suppression and the beneficial effects of short-chain fatty acids (SCFAs) like propionate on intestinal tumors, VA may be considered as an ideal option for effectively reducing high LA levels within the TME. In addition, some characteristics of many microorganisms include natural tumor targeting; for example, anaerobic bacteria such as VA can spontaneously target the tumor hypoxic microenvironment, and *Staphylococcus aureus* can effectively target

<sup>1</sup>Academy of Medical Engineering and Translational Medicine, Medical College, Tianjin University, Tianjin 300072, China. <sup>2</sup>Medical College, Linyi University, Linyi 276000, China.

\*Corresponding author. Email: jixiaoyuan@tju.edu.cn

†These authors contributed equally to this work.

the tumor inflammatory microenvironment (29, 32–35). Therefore, based on the unique properties of human symbiotic microorganisms, efficient tumor treatment strategies can be constructed through simple chemical or physical modifications (26, 29, 32, 34, 35).

In this study, we constructed an intelligent tumor treatment microrobot based on the unique physiological structure and metabolic characteristics of VA. First, the tetravalent piezoelectric ceramic material  $\text{BaTiO}_3$  (BTO) nanocubes were synthesized by a hydrothermal method, and then the membrane of *S. aureus* (SAM) was coated on their surface (SAM@BTO). This not only enables active tumor targeting but also provides a reactive site for modifying BTO elements to the VA surface. Next, SAM@BTO was encapsulated on the surface of VA cells (VA-SAM@BTO) using a classic click chemical reaction to build a multidirectional collaborative treatment platform for tumors. The inflammatory targeting of the SAM and the anaerobic targeting of VA cells provide the driving force of tumor double targeting and tumor penetration. After oral administration, it can accurately target orthotopic colorectal cancer (CRC) and achieve long-lasting retention and tumor penetration. Under in vitro ultrasonic (US) stimulation, BTO can catalyze two reduction reactions ( $\text{O}_2 \rightarrow \cdot\text{O}_2^-$  and  $\text{CO}_2 \rightarrow \text{CO}$ ) and three oxidation reactions ( $\text{H}_2\text{O} \rightarrow \cdot\text{OH}$ , GSH  $\rightarrow$  GSSG, and LA  $\rightarrow$  PA) simultaneously by virtue of its efficient piezoelectric effect. The proliferation of reactive oxygen species (ROS) and CO synergistically induces immunogenic death of tumor cells and activates the immune response. BTO catalyzes the oxidative LA coupling of VA cells to metabolize LA, completely disrupting the immunosuppressed microenvironment caused by high LA and effectively improving DC cell maturation and macrophage M1 polarization, increasing the proportion of effector T cells and decreasing the number of  $\text{T}_{\text{reg}}$  cells. Overall, this study presents a perspective on the design of biological hybrid microrobots and their potential application in regulating the tumor immunosuppressive microenvironment and mediating tumor multidirectional synergistic therapy.

## RESULTS

### Preparation and characterization of VA-SAM@BTO

Biological hybrid microrobots (VA-SAM@BTO) were prepared by synthesizing BTO, coating SAM on the surface of BTO, and loading SAM@BTO onto the surface of VA (Fig. 1). Given the excellent piezoelectric properties and piezoelectric catalytic performance of BTO, it has been selected as a tumor catalytic killing element (36). First, tetragonal BTO nanocubes were synthesized by a hydrothermal method, with  $\text{Ba}(\text{NO}_3)_2$  and  $\text{Ti}(\text{Bu})_4$  as the main raw materials. Transmission electron microscopy (TEM) images revealed that the diameter of BTO particles was approximately 10 nm (Fig. 2A). As clearly shown in the high-resolution TEM (HRTEM) image (fig. S1A), a high degree of crystallinity is suggested by the lattice fringes of a single particle with an interplanar spacing of  $d$  (110) = 2.82 Å, which is consistent with a perovskite crystal structure. The polar vectors along the [001], [110], and [111] planes corresponding to the tetragonal, orthorhombic, and rhombohedral phases of BTO are depicted in fig. S1B. To improve the water dispersibility of the nano platform, the hydrophobic BTO nanocubes were surface-coated with PEG-5000 (polyethylene glycol, molecular weight 5000). The successful preparation of PEG-modified BTO was verified using x-ray photoelectron spectroscopy (Fig. 2C and fig. S2).

The coordination environment was further elucidated through the x-ray absorption fine structure (fig. S3). Particularly, two distinct yet closely positioned peaks at  $2\theta \approx 45^\circ$  (where  $\theta$  represents the angle between an incident x-ray beam and the crystallographic reflecting plane) were observed in an x-ray diffractometer after the surface modification, confirming the preservation of the tetragonal structure of BTO, which matches well with the tetragonal piezoelectric BTO structure (JCPDS data no. 05-0626) (Fig. 2D and fig. S4).

In light of the affinity between *S. aureus* and the inflammatory microenvironment in CRC, we used the *S. aureus* cell membrane (SAM) to encapsulate BTO for targeted chemotaxis to inflammatory sites within the CRC intestine (37). An EZElisa Toxic shock syndrome toxin (TSST-1) ELISA Kit was used to measure the residual TSST in the SAM. As shown in fig. S5, the residual TSST in the SAM was not detectable. The limit of detection of this TSST Kit is 0.2 to 8 ng/ml; thus, there are less than TSST (0.2 ng/ml) remaining in the SAM, meeting the requirements of in vivo experiments regarding TSST. From the TEM image in Fig. 2A, it can be seen that the SAM vesicles measured approximately 100 nm in size, and the SAM@BTO structure displayed a distinctive core-shell morphology. Subsequently, we used a copper-free click chemistry approach to modify the VA surface with SAM@BTO (38). This process involves initially modifying the surface of VA with azido *N*-hydroxysuccinimide (NHS) ester, followed by conjugation with dibenzocyclooctyne (DBCO)-modified SAM-coated BTO nanoparticles using click chemistry (39). The functionalized modification of VA by SAM@BTO was confirmed through observations in the TEM and scanning electron microscopy images (Fig. 2A and fig. S6). Furthermore, our results revealed that when the VA concentration was  $1 \times 10^8$  and the BTO concentration was 0.1 mg/ml, the BTO nanoparticles exhibited excellent encapsulation on the VA surface. In addition, energy-dispersive x-ray spectroscopy and TEM elemental mapping confirmed the presence of barium (Ba), titanium (Ti), phosphorus (P), oxygen (O), and nitrogen (N) signals from VA-SAM@BTO, indicating that SAM@BTO was successfully and uniformly anchored onto the bacterial surfaces (Fig. 2B). Further insights into the structural features of VA-SAM@BTO were revealed by Fourier transform infrared spectroscopy, which found new absorption peaks at 1446, 1238, and  $752 \text{ cm}^{-1}$ , corresponding to the characteristic absorption peaks of pentacyclic 1,2,3-triazole produced by the azide-alkyne clicking reaction (Fig. 2E). The successful synthesis of VA-SAM@BTO was also confirmed through UV-visible spectroscopy analysis (fig. S7). Western blot analysis demonstrated that the extraction and encapsulation process had minimal effect on protein A on the biomimetic membrane (Fig. 2F). Moreover, alterations in size and surface charge after SAM@BTO modification were measured using dynamic light scattering, which showed a slight increase in diameter and a decrease in  $\zeta$ -potential (Fig. 2, G and H). Stability studies in water, phosphate-buffered saline (PBS), and Dulbecco's modified Eagle's medium indicated that VA-SAM@BTO could maintain its size over a 1-week observation period, suggesting good stability of the system (fig. S8). In conclusion, the diverse technical confirmations provide compelling evidence for the successful functionalization of SAM@BTO on the surface of VA. The method is demonstrated to be simple and efficient, yielding a VA-SAM@BTO biohybrid system with good stability. These findings underscore the successful application of copper-free click chemistry in modifying SAM@BTO onto VA, suggesting its potential for various biomedical and therapeutic applications. Furthermore, the prepared VA-SAM@BTO

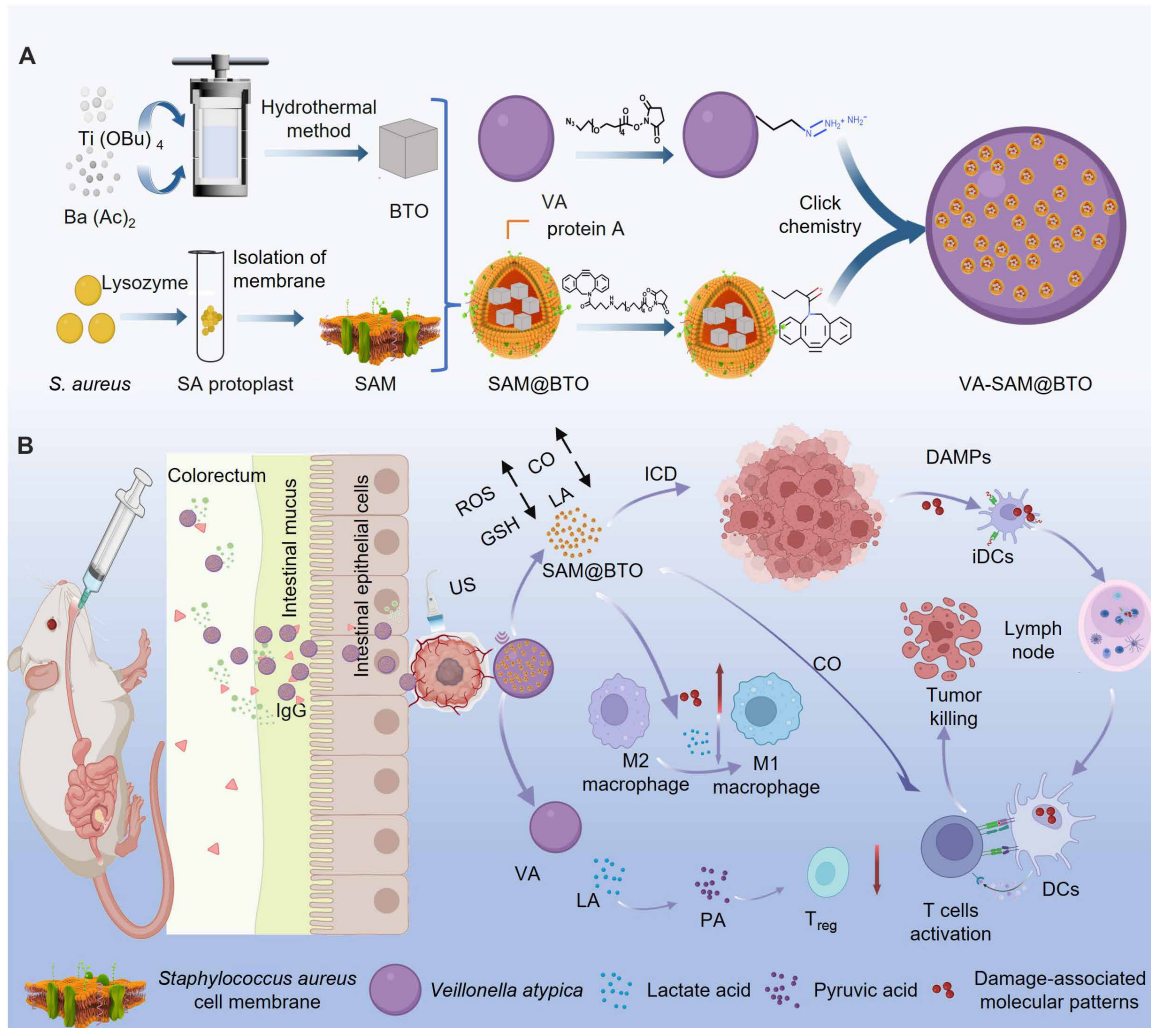


**Fig. 1.** A schematic diagram of a biological hybrid robot based on VA-SAM@BTO for oral targeted therapy of colorectal cancer. **(A)** Schematic for the preparation of VA-SAM@BTO. **(B)** Oral administration of VA-SAM@BTO induces catalytic and immunotherapeutic effects on orthotopic CRC mice.

biohybrid systems are anticipated to offer a promising strategy for targeted drug delivery and imaging applications.

### Biological characteristics of VA-SAM@BTO

Maintaining high bacterial viability is crucial for VA to target hypoxic areas of tumors (40). After modifying the functional group SAM@BTO of VA, we conducted experiments to assess the viability of bacterial cells and their ability to consume LA. The results showed similar amounts of bacterial colonies on agar plates between the VA and VA-SAM@BTO groups, indicating that the assembled SAM@BTO had negligible cytotoxic effects on VA cells (Fig. 2I and fig. S9). We also evaluated the metabolic performance of VA-SAM@BTO by adding LA to the bacterial culture medium. After 24 hours of incubation, the LA concentration was reduced to approximately 30% and further decreased to approximately 50% of the initial level after 48 hours. There was no significant difference in LA metabolism between the two groups, indicating that VA-SAM@BTO maintained its superior bioactivity and ability to transform LA (Fig. 2J). In

addition, the absorption of orally administered drugs in the gastrointestinal tract is crucial for their effectiveness (41, 42). In this study, we evaluated the viability of VA and VA-SAM@BTO in simulated gastric fluid and intestinal fluid. As shown in Fig. 2K, agar plate cultures were used to observe the growth of the formulation on solid media after the gastric and intestinal fluid experiments were simulated to obtain more accurate information on bacterial viability. We found that functionalization with SAM@BTO enhanced the ability of VA to survive through gastric acid. This finding suggests that SAM@BTO protects VA from the acidic environment of the stomach and enhances its survivability in the harsh conditions of the gastrointestinal tract.

There is substantial evidence supporting the notion that bacteria have the ability to navigate specific biological environments and overcome complex biological barriers. As demonstrated in Fig. 2 (L to M), our in vitro hypoxia model experiments showed that both VA and VA-SAM@BTO effectively targeted hypoxic conditions. Under normoxic conditions, VA exhibited relatively low migration through

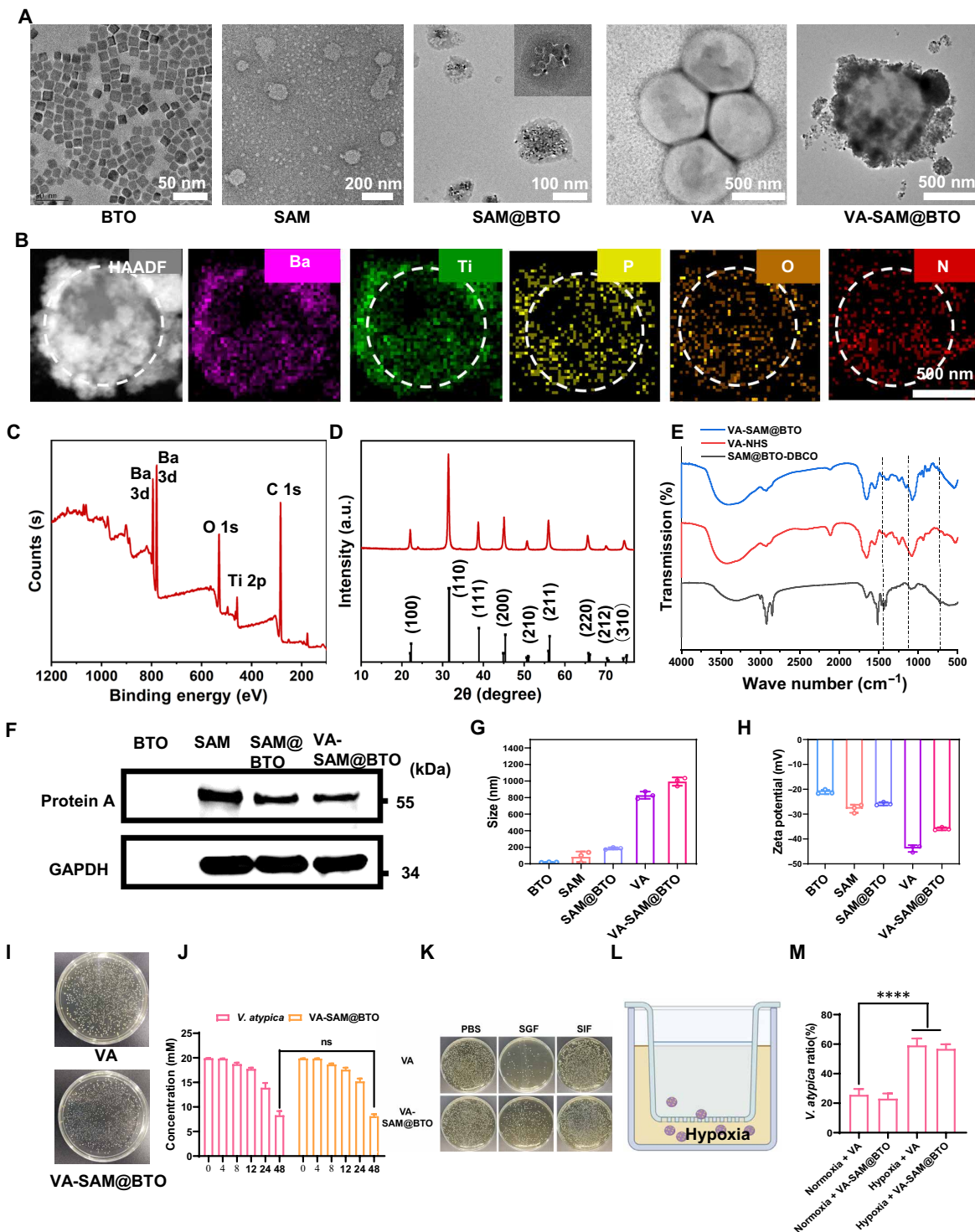


**Fig. 2. Characterization of VA-SAM@BTO.** (A) TEM images of BTO, SAM, SAM@BTO, VA, and VA-SAM@BTO. (B) High-angle annular dark-field (HAADF) and mapping images of VA-SAM@BTO. (C) X-ray photoelectron spectroscopy and (D) x-ray diffractometer spectrum of PEG-modified BTO. (E) Fourier transform infrared analysis of SAM@BTO-DBCO, VA-NHS, and VA-SAM@BTO. (F) Western blot analysis of protein A in BTO, SAM, SAM@BTO, and VA-SAM@BTO. GAPDH, glyceraldehyde-3-phosphate dehydrogenase. (G) Dynamic light scattering and (H) zeta potential analysis of differently treated nanoparticles. (I) Digital photos of VAs in culture media plates with or without VA-SAM@BTO treatment. (J) LA consumption detection of VA and VA-SAM@BTO. (K) The activity of different samples in simulated gastrointestinal fluid. (L) Schematic illustration of the hypoxia model. (M) The ratio of bacteria in the bottom chamber was calculated after the cells had migrated at 37°C for 60 min ( $n = 3$ ). Statistical significance was determined using one-way analysis of variance (ANOVA) followed by Tukey's multiple comparison test (ns represents not significant; \*\*\*\* $P < 0.0001$ ).

the polycarbonate membrane, with less than 30% of the bacteria reaching the bottom chamber after a 120-min migration period. However, under hypoxic conditions, the number of VAs in the bottom chamber markedly increased to more than 60%. VA-SAM@BTO displayed a similar trend, indicating that the presence or absence of SAM@BTO did not alter the hypoxic tendency of VA.

These findings indicate that the functionalization of VA with SAM@BTO does not have a negative impact on the viability and metabolic activity of VA. In addition, it enhances their tolerance to gastric acid and maintains their ability to target hypoxic environments. These results suggest that VA-SAM@BTO can withstand the challenges of the gastrointestinal environment, offering promising potential for its application as an oral drug delivery system in various biomedical and therapeutic approaches.

### Catalytic performance and mechanism of VA-SAM@BTO

BTO serves as the functional component in biohybrid microrobots, functioning as a classic piezoelectric material. It is characterized by strong inversion symmetry breaking and spontaneous polarization, which can be switched by external electric fields (43). This property enables BTO to generate a piezoelectric effect, thereby inducing catalytic behavior (Fig. 3A). We used electron spin resonance (ESR) spectroscopy to verify the production of •OH and superoxide anions under US irradiation for BTO, SAM@BTO, and VA-SAM@BTO. As depicted in Fig. 3B, BTO, when subjected to US, generated •OH, and the presence of •OH resulted in the formation of characteristic peaks of 2,2,6,6-tetramethylpiperidine (DMPO) with an intensity ratio of 1:2:2:1. Moreover, Fig. 3C demonstrates that the generation of •O<sub>2</sub><sup>-</sup> led to the appearance of six peaks in the ESR spectrum of DMPO. Furthermore, the encapsulation of SAM on BTO, as well as the functionalization of VA, did not affect the piezoelectric catalytic generation of •OH and •O<sub>2</sub><sup>-</sup> by BTO.

We conducted a comprehensive study on the catalytic behavior of BTO in the presence of external US irradiation (43). Initially, we used DPBF as a probe to examine the generation of •O<sub>2</sub><sup>-</sup>. The results depicted in Fig. 3 (D to F) show minimal variation in DPBF absorbance when solely using BTO or applying US treatment independently. However, upon combining ultramicrotometer-sized BTO with US treatment, the absorption of DPBF at OD<sub>410</sub> gradually decreased with increasing US time, indicating a gradual increase in the •O<sub>2</sub><sup>-</sup> content. Furthermore, similar to the ESR results, the application of SAM on BTO and the functionalization modification of VA did not significantly affect the production of •O<sub>2</sub><sup>-</sup>. In addition, we used the COP-1 probe to measure CO generation through CO<sub>2</sub> reduction via BTO piezoelectric catalysis (Fig. 3G). As depicted in Fig. 3 (H and I), similar to the production of •O<sub>2</sub><sup>-</sup>, no CO was detected when using only BTO or US treatment. However, when BTO was combined with US excitation, CO<sub>2</sub> reduction commenced. Both SAM@BTO and VA-SAM@BTO demonstrated similar efficiencies in CO generation.

In this study, we first confirmed that BTO can catalyze two reduction reactions synchronously by using excitation electrons under the action of US. Next, we continue to explore whether BTO holes can catalyze the oxidation reaction with their powerful oxidation effect. Rhodamine B (RhB) was used as a probe to assess the effectiveness of BTO piezoelectric catalysis in oxidizing H<sub>2</sub>O to produce •OH radicals (Fig. 3J). As depicted in Fig. 3 (K and L) and fig. S10, the combined application of BTO and US led to a gradual decrease in the absorption peak intensity of RhB with increasing US

exposure. This observation suggests a significant capacity for generating •OH radicals compared to using BTO alone or US treatment alone. Furthermore, both SAM@BTO and VA-SAM@BTO demonstrated similar •OH generation capabilities under US excitation. Then, we used the glutathione (GSH) assay kit as a probe to evaluate the catalytic oxidation of GSH induced by BTO piezoelectric stimulation (Fig. 3M). As illustrated in Fig. 3 (N to O) and fig. S11, when only BTO or US treatment was applied independently, the GSH level remained nearly unchanged. However, upon US excitation, the absorption peak of GSH gradually decreased, indicating a substantial consumption of GSH resulting from the combined effect of BTO and US. In addition, both SAM@BTO and VA-SAM@BTO demonstrated similar decreasing trends in GSH levels under ultrasound stimulation. Last, we investigated the piezoelectric catalysis of LA oxidation by BTO (Fig. 3P). As depicted in Fig. 3 (Q and R), BTO effectively oxidizes/depletes LA in a manner dependent on the power of US stimulation. As anticipated, SAM@BTO and VA-SAM@BTO demonstrated similar trends under US exposure. As anticipated, SAM@BTO and VA-SAM@BTO demonstrated similar trends under US exposure. Furthermore, as depicted in fig. S12 (A and B), BTO generates holes after US stimulation, enabling it to oxidize NADH (reduced form of nicotinamide adenine dinucleotide) to NAD<sup>+</sup> [nicotinamide adenine dinucleotide (oxidized form)]. Further investigations were conducted to evaluate the LA consumption ability of VA-SAM@BTO under multiple US stimulations. The results demonstrated that the VA-SAM@BTO + US group exhibited the greatest ability to consume LA. This is mainly due to the reaction between the holes generated in BTO and NADH, which oxidizes NADH to NAD<sup>+</sup>. Subsequently, the produced NAD<sup>+</sup> promotes LA metabolism via VA, thereby accelerating LA consumption (fig. S12C).

These research findings demonstrate that BTO can undergo spontaneous polarization and generate piezoelectric catalytic effects under US. Not only can it reduce O<sub>2</sub> to •O<sub>2</sub><sup>-</sup> and CO<sub>2</sub> to CO but it can also oxidize H<sub>2</sub>O to •OH, GSH to GSSG, and LA to PA. Note also that the SAM coating and VA connection have no significant impact on the piezoelectric catalytic efficiency of BTO. Therefore, BTO's sensitivity to US irradiation reflects its highly controllable catalytic performance triggered by US, making it an efficient sonosensitizer for SDT cancer treatment.

### Anticancer abilities of VA-SAM@BTO *in vitro*

The biological hybrid microrobots VA-SAM@BTO exhibit powerful catalytic activity and LA consumption capability, which prompted us to explore their potential cytotoxicity for cancer cells (44). We explored the interaction between VA-SAM@BTO and tumor cells using a porous transmembrane plate with Caco-2 cells. CT26 cells were cultured in the bottom layer, while different materials were added to the upper porous plate. After cultivation under anaerobic conditions, we assessed cell viability using a CCK-8 assay. As shown in Fig. 4A, even at a concentration of 100 µg/ml, SAM@BTO displayed minimal cytotoxicity to CT26 cells, indicating its low inherent cytotoxicity. However, with increasing doses of SAM@BTO and subsequent 5 min of US treatment, cell viability gradually decreased, reaching approximately 30% at a concentration of 100 µg/ml. Subsequently, we evaluated the cytotoxicity of different formulations (including SAM@BTO, VA, US, SAM@BTO + US, and VA-SAM@BTO + US) on tumor cells. As illustrated in Fig. 4B, compared to the control group, SAM@BTO and VA-SAM@BTO exhibited significant cytotoxicity under US treatment, whereas only VA led to slight

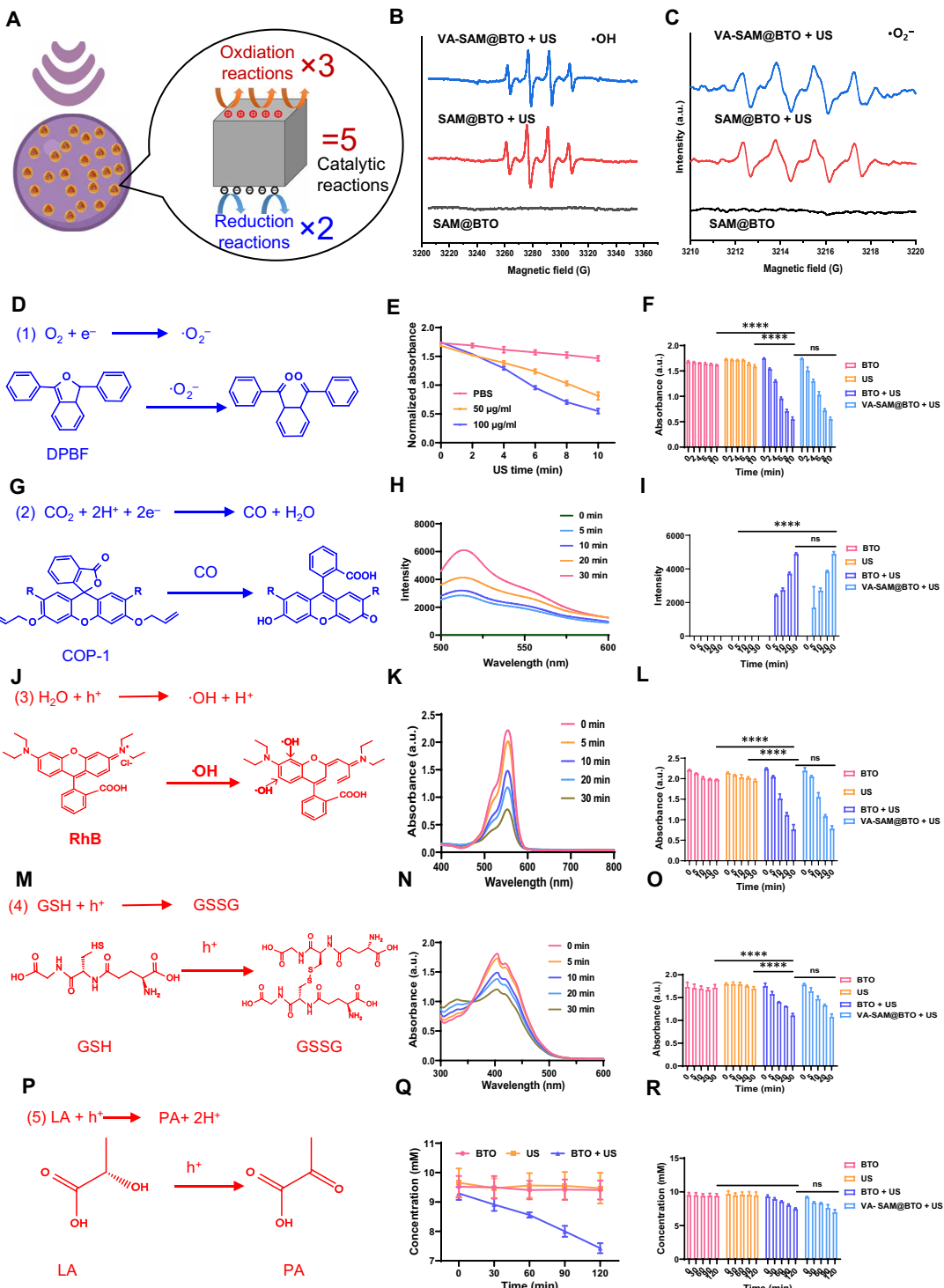


**Fig. 3. Catalytic performance and mechanism of VA-SAM@BTO.** (A) Schematic showing the catalytic mechanism of VA-SAM@BTO under US irradiation. Single (B) •OH and (C) •O<sub>2</sub><sup>-</sup> generated under US irradiation. The mechanism (D) and performance (E and F) of •O<sub>2</sub><sup>-</sup> generation with US-excited electrons. Schematic (G) and performance (H and I) of CO generation with US-excited electrons. The mechanism (J) and performance (K and L) of •OH generation with US-excited holes. The mechanism (M) and performance (N and O) of GSH consumption with US-excited holes. The mechanism (P) and performance (Q and R) of LA consumption with US-excited holes. All results are presented as the means ± SD ( $n = 3$ ). Statistical significance was determined using ANOVA followed by Tukey's multiple comparison test (\*\*P < 0.001, \*\*\*P < 0.0001).

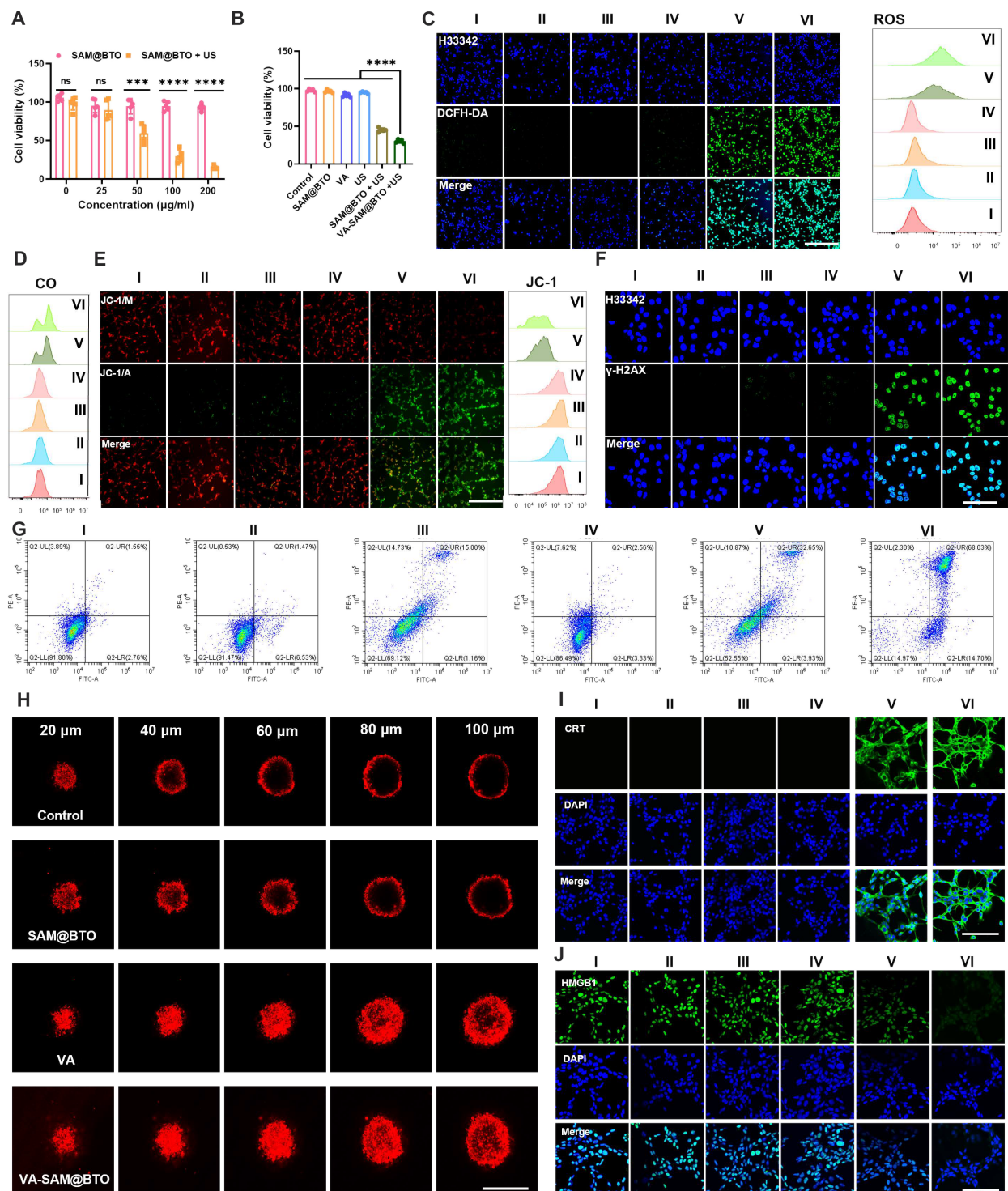


**Fig. 4. The biocompatibility and cytotoxicity of VA-SAM@BTO.** (A) The cytotoxicity of SAM@BTO and SAM@BTO + US treatment to CT26 cells ( $n = 5$ ). (B) The cytotoxicity of different treatments toward CT26 cells ( $n = 5$ ). (C) DCFH-DA staining and flow cytometry analysis detecting intracellular ROS generation. Scale bar, 500  $\mu\text{m}$ . (D) Flow cytometry analysis detecting intracellular CO generation. (E) Mitochondrial membrane potential and flow cytometry analysis detecting changes in the intracellular mitochondrial membrane potential. Scale bar, 300  $\mu\text{m}$ . (F) Early DNA damage. Scale bar, 100  $\mu\text{m}$ . (G) Flow cytometry analysis detecting the apoptotic behaviors of CT26 cells. (H) Z-stack CLSM images of 3D CT26 cell spheroids at different distances. Scale bar, 300  $\mu\text{m}$ . (I) CLSM images of the release of CRT after different treatments. Scale bar, 50  $\mu\text{m}$ . (J) CLSM images showing the release of HMGB1 after different treatments. Scale bar, 50  $\mu\text{m}$ . I: PBS, II: SAM@BTO, III: VA, IV: US, V: SAM@BTO + US, VI: VA-SAM@BTO + US. Statistical significance was determined using ANOVA followed by Tukey's multiple comparison test (\*\* $P < 0.001$  and \*\*\*\* $P < 0.0001$ ). DAPI, 4',6-diamidino-2-phenylindole.

cell death due to its promotion of tumor growth through LA consumption (fig. S13). This highlighted the superior killing ability of VA-SAM@BTO against tumor cells.

Next, we explored the potential mechanisms underlying the potent cytotoxic effects of VA-SAM@BTO on CT26 tumor cells. First, we used the 2',7'-dichlorodihydrofluorescein diacetate (DCFH-DA) probe to monitor the generation of intracellular ROS. As depicted in Fig. 4C, when cells were exposed to US, VA, or SAM@BTO individually, no significant green fluorescence was detected. However, intense green fluorescence was observed in the SAM@BTO + US group, and a comparable level of green fluorescence was also present in the VA-SAM@BTO + US group. According to the flow cytometry analysis of ROS generation under different treatments, the intracellular ROS levels were significantly increased after treatment with SAM@BTO or VA-SAM@BTO in the US. Furthermore, we used the COP-1 probe to examine the generation of intracellular CO, as shown in Fig. 4D and fig. S14. Prominent green fluorescence was evident in the SAM@BTO + US and VA-SAM@BTO + US groups, whereas this phenomenon was not observed in the SAM@BTO, US, and VA alone groups. The trends observed in the flow cytometry experiments were almost identical to those observed using confocal laser scanning microscope (CLSM), which provided further evidence that materials exposed to US can generate a significant amount of CO. These findings indicate that, owing to the robust piezoelectric catalytic ability of BTO, both SAM@BTO and VA-SAM@BTO are capable of converting CO<sub>2</sub> into CO under the influence of US. Subsequent validation at the cellular level confirmed that the encapsulation of SAM and the functional modification of VA do not impede the catalytic performance of BTO.

Excess ROS directly damages DNA double strands in the cell nucleus (45). Similarly, an excess of intracellular CO directly alters the polarization potential of the mitochondrial membrane of tumor cells, leading to early DNA damage and mitochondrial membrane damage and promoting apoptosis of tumor cells (46). We assessed mitochondrial dysfunction by monitoring the changes in mitochondrial membrane potential (MMP) using the JC-1 fluorescent probe. As depicted in Fig. 4E, in cells treated with SAM@BTO alone, the majority of cells were stained with JC-1 aggregates, indicating minimal MMP changes, similar to normal cells. However, under US irradiation, cells treated with SAM@BTO and VA-SAM@BTO exhibited significantly increased green fluorescence, indicating mitochondrial depolarization. To further elucidate US-driven therapy-mediated DNA damage, we used γ-H2AX as a DNA damage marker to study the effects of different treatments on DNA. As shown in Fig. 4F, no significant green fluorescence was observed in the PBS group, US group, or VA group. However, significant green fluorescence was observed in the SAM@BTO + US and VA-SAM@BTO + US groups, indicating severe DNA damage in CT26 cells.

To gather more reliable evidence, we evaluated the in vitro anti-tumor performance of the VA-SAM@BTO biohybrid system using live/dead cell staining and apoptosis assay kits. As depicted in fig. S15, neither individual US irradiation nor SAM@BTO treatment alone exhibited significant cytotoxicity toward CT26 cells. VA treatment alone led to minimal cell death; however, when combined with US irradiation, the majority of tumor cells were killed, demonstrating the superior protumor cytotoxic effect of VA-SAM@BTO under US irradiation. Similarly, as shown in Fig. 4G, flow cytometry analysis of apoptosis revealed that SAM@BTO treatment alone did not demonstrate significant cytotoxicity, suggesting its good

biocompatibility. The increased apoptosis rate in the SAM@BTO + US group indicated significant SDT-related apoptosis, while the higher tumor cell apoptosis rate in the VA-SAM@BTO + US group suggested a better antitumor effect. These results further validate the designed VA-SAM@BTO biohybrid system's capability to generate ROS and CO in response to US, effectively consume intracellular LA, and promote tumor cell apoptosis, thereby demonstrating a significant in vitro antitumor killing effect.

We have conducted further research on our biohybrid microrobots with the objective of deeply penetrating tumors and enhancing antitumor effects using three-dimensional tumor spheres. As depicted in Fig. 4H, after coculturing with SAM@BTO, VA, SAM@BTO, or VA-SAM@BTO, we observed varying degrees of penetration into the three-dimensional tumor spheres, as indicated by the presence of red fluorescence. Specifically, following SAM@BTO treatment, only weak fluorescence was detected at the periphery of the tumor spheres. Because of VA's strict anaerobic nature, it was able to penetrate deeply into the cell aggregates within the tumor sphere, reaching a distance of 80 μm. The combination of SAM@BTO and VA resulted in the greatest penetration depth. In addition, as shown in fig. S16, we observed significant penetration of the tumor spheres in the SAM@BTO + US and VA-SAM@BTO + US groups, leading to significant cell damage through the generation of ROS and CO within the tumor spheres. Note that the VA-SAM@BTO + US group induced the most severe cell death, highlighting the ability of our biohybrid robots to deeply penetrate the depths of tumors and produce potent antitumor effects.

### Immunological effect of VA-SAM@BTO in vitro

After confirming that VA-SAM@BTO induces cytotoxic effects on tumor cells through its piezoelectric catalysis and LA metabolism, we eagerly evaluated its potential for tumor immune activation. Initially, calreticulin (CRT) exposure and HMGB1 release from CT26 cells after different treatments were observed via CLSM (Fig. 4, I and J). The percentages of CRT (green fluorescence) in the VA-SAM@BTO + US group were obviously greater than those in the PBS or US-only groups, while the percentages of HMGB1 were significantly lower than those in the PBS or US-only groups, suggesting that the combination of VA-SAM@BTO with US could induce effective ICD. Moreover, we investigated the innate immune response of macrophages (RAW 264.7) and the maturation status of DCs in vitro. Cocultures of differently pretreated CT26 cells with macrophages were conducted for 24 hours using a transwell system, and the phenotype of macrophages was assessed by evaluating the expression of characteristic markers. Compared to the other groups, RAW 264.7 macrophages cocultured with CT26 cells pretreated with VA alone exhibited significant red fluorescence and higher levels of the M1 marker CD86, indicating that VA uptake of LA in the microenvironment inhibited the M2 phenotype activity of macrophages and promoted their polarization toward the M1 phenotype (Fig. 5A). In addition, the group treated with SAM@BTO + US alone showed a significant up-regulation of M1 markers achieved through immunogenic cell death of tumor cells. Furthermore, the VA-SAM@BTO + US group demonstrated the strongest M1 polarization capability, as confirmed by flow cytometry analysis (Fig. 5, B and C, and figs. S17 and S18). This provides evidence that VA-SAM@BTO + US affects the LA metabolism of tumor cells, resulting in immunogenic cell death and promoting the polarization of macrophages from the M2 subtype to the M1 subtype.

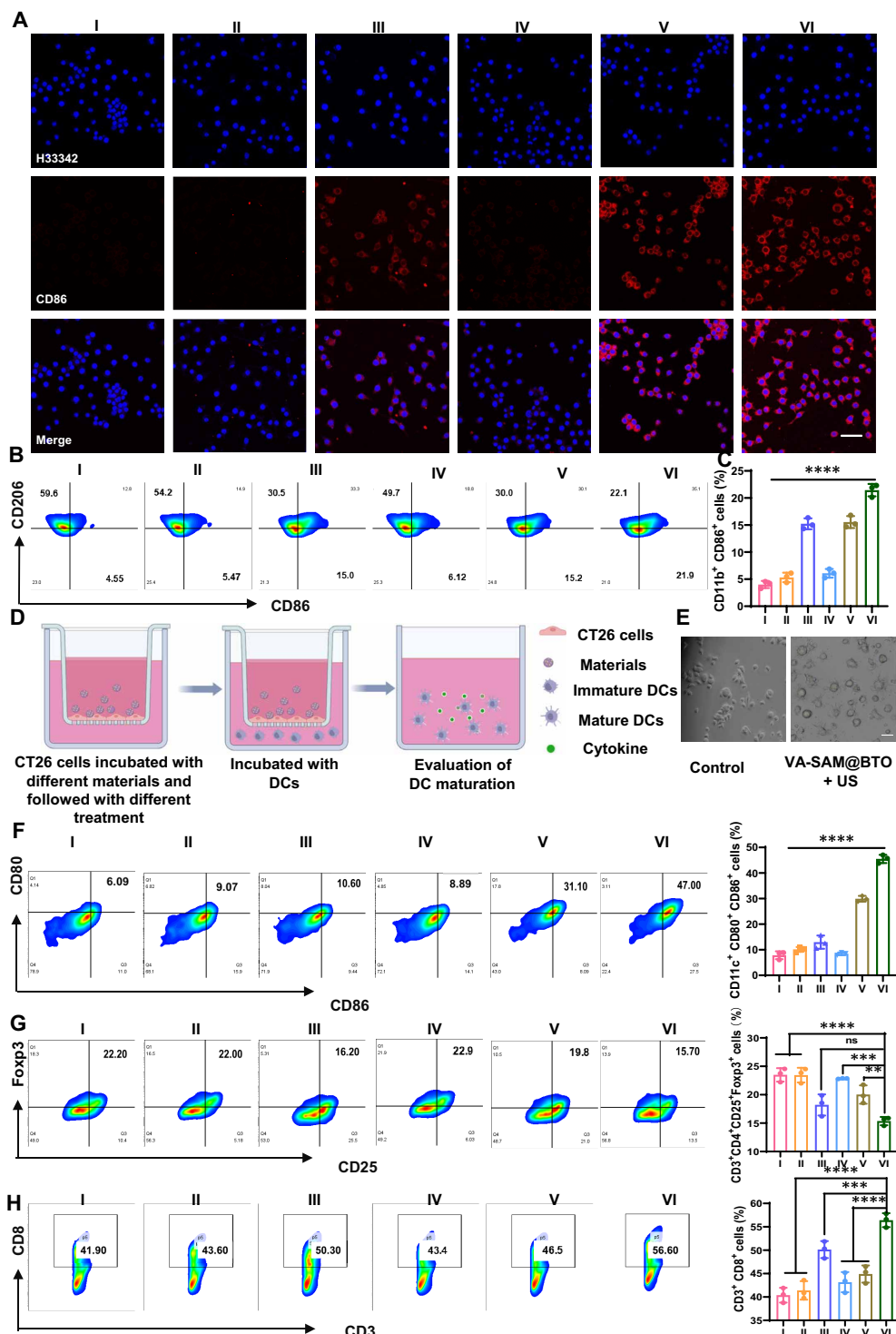


**Fig. 5. In vitro immune activities of VA-SAM@BTO.** (A) CLSM images and (B) flow cytometry analysis of RAW264.7 cells. Scale bar, 100  $\mu$ m. (C) Flow cytometry analysis of CD86<sup>+</sup> RAW264.7 cells. (D) Schematic diagram of the in vitro immunological experiments. (E) Microscopy image of DCs. Scale bar, 100  $\mu$ m. Flow cytometry results and quantification of the percentages of (F) DCs, (G) T<sub>reg</sub>, and (H) CD8<sup>+</sup> T cells detected by flow cytometry. All the results are presented as the means  $\pm$  SD ( $n = 3$ ). I: PBS, II: SAM@BTO, III: VA, IV: US, V: SAM@BTO + US, VI: VA-SAM@BTO + US. Statistical significance was determined using ANOVA followed by Tukey's multiple comparison test (\*\* $P < 0.01$ , \*\*\* $P < 0.001$ , and \*\*\*\* $P < 0.0001$ ).

DCs play a crucial role in initiating, regulating, and maintaining immune responses. Highly immunogenic tumor cells can rapidly trigger the maturation of DCs, further activating adaptive immune responses (47). Freshly isolated bone marrow–derived DCs were cocultured with pretreated CT26 cells, followed by staining for flow cytometric analysis to assess the ability of tumor cells to induce DC maturation under different treatments (Fig. 5D). It was clearly observed that immature DCs exhibited significantly increased surface synapses after coculturing with tumor cells treated with VA-SAM@BTO + US for 3 hours, indicating an elevated level of maturation (Fig. 5E). Furthermore, compared with cancer cells treated only with US or VA, these cancer cells stimulated by the chemo-catalytic therapy SAM@BTO + US significantly promoted DC maturation, with the percentage of mature DCs (CD11c<sup>+</sup>CD80<sup>+</sup>CD86<sup>+</sup> cells) reaching 31.10% after coculture. Notably, because of the partial ablation of VA by US treatment, which functions similarly to an immune adjuvant, VA-SAM@BTO further enhanced DC maturation, with the highest level of DC maturation (47.00%) triggered by the combination treatment of tumor cells (Fig. 5F and fig. S19).

It has been reported that tumor cells not only deprive effector T cells of nutrients by creating a metabolite-deficient microenvironment to evade “pursuit” but also provide LA to T<sub>reg</sub>s, uniting “allies” to jointly resist effector T cells (10). Therefore, we hypothesized that reducing the LA levels in tumor cells may help disrupt the metabolic symbiosis between tumor cells and T<sub>reg</sub> cells, thereby reducing the barrier of Treg cells in tumor immunity and enhancing the cytotoxic function of effector T cells. Consequently, we investigated the regulatory effects of VA-SAM@BTO on T cells. As shown in Fig. 5G and fig. S20, the VA-SAM@BTO + US combination treatment group significantly reduced the infiltration of T<sub>reg</sub>s in the tumor compared to the other groups. This suggests that VA significantly inhibits the activity of Treg cells by consuming LA, while SAM@BTO + US shows mild inhibition of Treg cells due to the immunomodulatory effect of CO and oxidation of LA. In addition, as shown in Fig. 5H, the percentage of CD8<sup>+</sup> T cells in the VA-SAM@BTO + US group was approximately 1.4 times higher than that of the control group and 1.2 times higher than that of the SAM@BTO + US group, indicating that VA-SAM@BTO + US treatment suppressed the function of T<sub>reg</sub> cells in tumor immunity and enhanced the function of effector T cells.

### Tumor targeting and biological distribution of VA-SAM@BTO in vivo

To investigate the specific tumor targeting and colonization behavior of VA-SAM@BTO at the tumor site, we conducted an *in vivo* biodistribution study using an orthotopic CRC animal model. Female BALB/c mice with an orthotopic CRC model were orally administered VA-SAM@BTO at a dose of  $1 \times 10^8$  colony-forming units (CFUs). Various organs and tumor tissues were collected at different time points postinfusion. The collected samples were then homogenized and diluted for bacterial culture on Luria-Bertani agar plates to quantify CFUs. The results revealed a gradual decrease in bacteria from major organs (the heart, liver, spleen, lung, and kidney). In contrast, the CFU values in tumors exhibited a rapid increase over time (Fig. 6A and fig. S21). These findings suggest that VA-SAM@BTO can selectively colonize the hypoxic, immunosuppressive, and biochemically unique TME of tumors. Furthermore, to evaluate the long-term safety profile of VA-SAM@BTO in mouse organs, we conducted additional investigations into the bacterial

distribution at 360 and 720 hours (Fig. 6A and fig. S22). The findings revealed that by 360 hours, the number of viable bacteria in the mouse organs had significantly declined to very low levels, and by 720 hours, they were completely eliminated, likely attributed to effective clearance by the immune system. Note that the viable bacteria in various organs of healthy mice were rapidly cleared from all the extracted organs, indicating a favorable safety profile over the long term (Fig. 6B and fig. S23).

To convincingly demonstrate the *in vivo* tumor targeting ability, indocyanine green (ICG)-labeled SAM@BTO, VA, and VA-SAM@BTO were orally administered to BALB/c mice bearing CT26 orthotopic tumors, and the fluorescence distribution at different time points was monitored using a small animal fluorescence imaging system, as depicted in Fig. 6C. All three formulations exhibited varying degrees of targeting ability, which can be attributed to the SAM-responsive recruitment of IgG in the orthotopic CRC inflammatory environment and VA's affinity for tumor hypoxia and the high-nutrient environment. Furthermore, consistent with the results from plate coating results, VA-SAM@BTO demonstrated the highest level of targeting enrichment under dual targeting stimulation, showcasing a unique capability for selective colonization at the tumor site. The *ex vivo* fluorescence images of the tumor and different organs further validated the notable targeting accumulation ability of VA-SAM@BTO (Fig. 6D). In addition, as depicted in Fig. 6 (E and F), the results of the intestinal penetration experiment illustrate that following intestinal perfusion, the fluorescence images of the CRC intestinal segments demonstrate a substantial penetration of VA-SAM@BTO through the intestinal barrier, reaching the tumor site. The VA-SAM@BTO group exhibited a mean fluorescence intensity at the tumor site approximately 2.87 times higher than that of the SAM@BTO group.

Moreover, we performed additional experiments to examine the stability of the preparation in simulated gastric and intestinal fluids. As depicted in fig. S24, after a 2-hour incubation in artificial gastric fluid, the majority of the SAMs remained intact on the nanoplateform, indicating the resilience of the bacterial biomimetic membrane against gastric acid digestion. However, in the artificial colon fluid, there was evidence of some SAM shedding, as evidenced by the presence of free BTO. This finding suggested that there was partial detachment of the SAM in the colonic environment. Frozen biological TEM images of both normal intestine and orthotopic CRC tissues (Fig. 6G) provided compelling evidence that VA-SAM@BTO can effectively target tumor sites. Furthermore, as a result of partial SAM dissociation in the intestine, some free BTO particles were formed. Owing to their small size and hydrophilic nature, these particles were also capable of successfully reaching the tumor site. These findings offer valuable insights into the specific tropism and colonization behavior of VA-SAM@BTO in the TME. In recent years, advances in detection technology and our understanding of TMEs have provided increasing evidence of the presence of bacteria in tumors (48). The human gastrointestinal tract naturally hosts a diverse population of microorganisms. Consequently, detecting microorganisms in colorectal tumors is relatively easy, suggesting that gastrointestinal microorganisms may have the ability to penetrate the intestinal barrier and enter tumors (49). CRC is characterized by a highly inflammatory environment and disruption of the intestinal barrier, which may facilitate the entry of certain microorganisms and promote the colonization of other microorganisms within the tumor. Various factors can lead to the breakdown of the mucosal

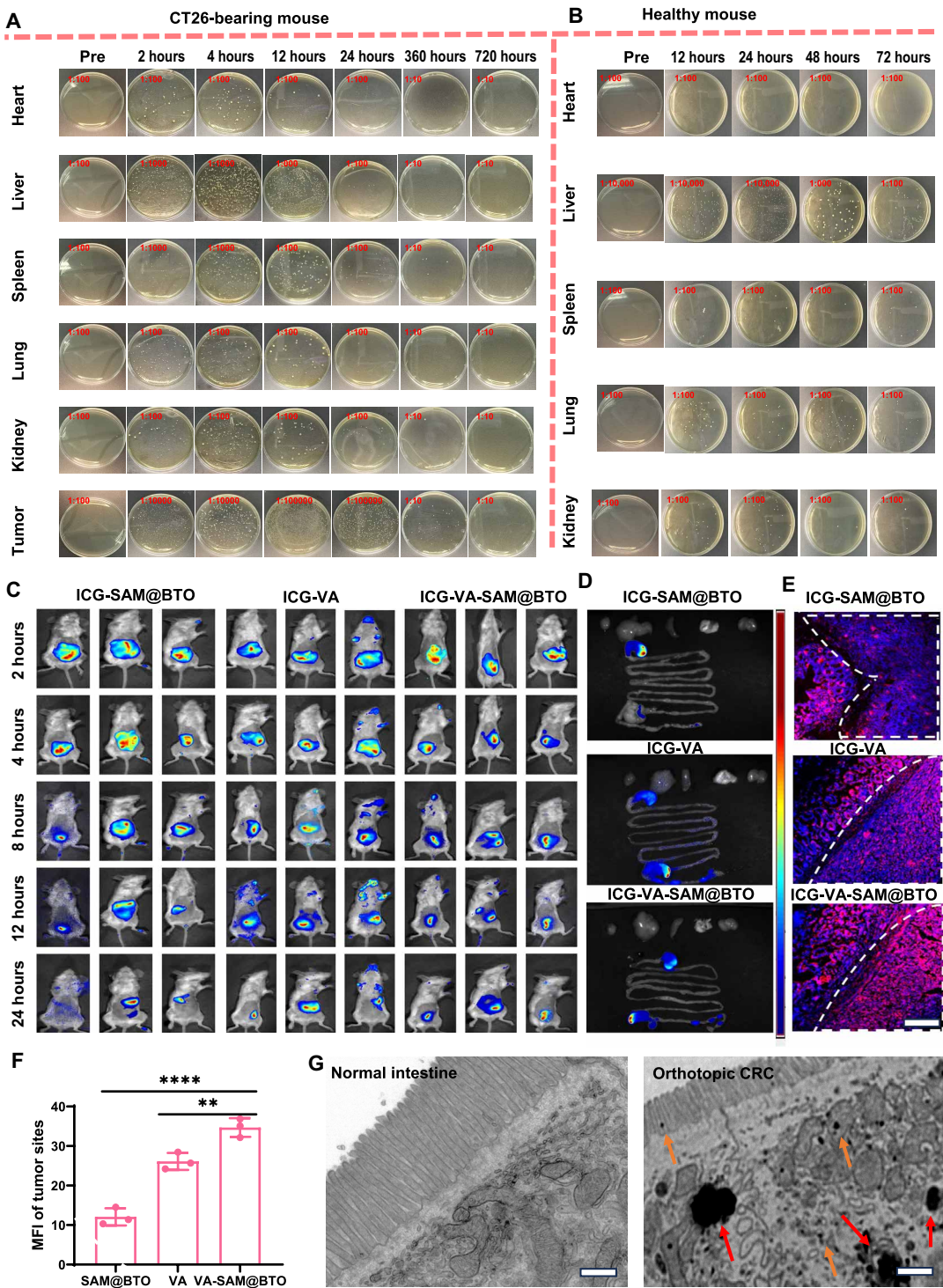


**Fig. 6. In vivo targeting distributions of VA-SAM@BTO.** (A and B) Representative photographs of solid Luria-Bertani agar plates showing bacterial colonization in different organs collected from orthotopic CRC mice and healthy mice at various time points after gavage of VA-SAM@BTO. (C) Following gavage administration of ICG-labeled SAM@BTO, VA, or VA-SAM@BTO, in vivo optical live imaging was conducted on orthotopic CRC mice at different time points. (D) Ex vivo quantification of the fluorescence intensity in orthotopic CRC mice after gavage with ICG-labeled SAM@BTO, VA, or VA-SAM@BTO. (E) In situ CLSM images of tumor colon segments following perfusion in orthotopic CRC mice. The white dashed line demarcates the tumor location. Scale bar, 250  $\mu$ m. (F) Quantification of fluorescence at the tumor site in each group ( $n = 3$ ). (G) In vivo morphology images of microparticles in the control group (A) and the VA-SAM@BTO group (B), with BTO marked with orange arrows and VA-SAM@BTO marked with red arrows. Scale bars, 1  $\mu$ m. All the results are presented as the means  $\pm$  SDs ( $n = 3$ ). Statistical significance was determined using ANOVA followed by Tukey's multiple comparison test (\*\* $P < 0.01$  and \*\*\*\* $P < 0.0001$ ).

barrier, allowing microorganisms to infiltrate the tumor (50). In this study, the recruitment of SAM to the CRC environment allowed the microrobots to successfully reach the cancer site. Furthermore, the recruitment of VA to the hypoxic and nutrient-rich TME resulting from rapid angiogenesis and tumor necrosis facilitated the effective delivery of the microparticles to the tumor site. In addition, several studies have demonstrated that orally administered bacteria can reach CRC incidence and exhibit significant antitumor effects (51, 52). In conclusion, the factors that promote tumor development and disrupt the mucosal barrier present an opportunity for our microrobots to contact tumors, thus enabling successful delivery to the tumor site. The selective colonization and tumor-targeting ability of this bacterial formulation show promise for potential applications in cancer therapy and targeted drug delivery.

### Anticancer abilities of VA-SAM@BTO in vivo

Considering the significant cancer cell-killing effect of VA-SAM@BTO + US in vitro, we evaluated its tumor suppression effect in vivo using the CT26-luc orthotopic mouse model (Fig. 7A). The mice were randomly divided into six groups and received the following treatments: PBS, SAM@BTO, VA, US, SAM@BTO + US, and VA-SAM@BTO + US. The tumor growth of the orthotopic CRC mice receiving different treatments was monitored by detecting bioluminescence from the tumor tissue using IVIS (Fig. 7B). The tumor inhibition rates for SAM@BTO and US used alone were only 5.26 and 6.42%, respectively. However, the SAM@BTO + US group showed moderate tumor regression efficacy. VA used alone also showed low tumor regression efficacy, while the VA-SAM@BTO + US group exhibited a high inhibition rate of up to 90.36% (Fig. 7C). In another CRC model, the MC38 tumor mouse model, after ultrasound treatment during in vivo therapy, led to a minor decrease in the activity of VA bacteria, but this change did not result in severe inhibition (fig. S25). In addition, similar antitumor effects were observed with different formulations (fig. S26). These findings indicate that the anticancer ability of VA-SAM@BTO may be applicable to other CRC models. We visually observed the colon cancer tumor volume in mice treated for 10 days using intraperitoneal endoscopy (Fig. 7D). Consistent with the bioluminescence results, we found that the combination therapy of VA-SAM@BTO + US displayed the highest tumor inhibition efficiency, followed by SAM@BTO + US. This was further confirmed by comparing the dissected mouse tumor tissue volume after 15 days of treatment (Fig. 7E). These results demonstrate that VA-SAM@BTO + US exhibits significant tumor suppression potential after four repeated administrations, and the microbial robot designed based on bacterial metabolism and catalytic therapy achieves a remarkable synergistic therapeutic effect. In addition, mice treated with VA-SAM@BTO + US had a significantly longer lifespan than the other groups, with all mice surviving longer than 30 days (Fig. 7F). These treatments did not significantly affect the body weight of the mice, indicating that the harmful effects on mouse health can be negligible (Fig. 7G).

In addition, as depicted in Fig. 7H, the results of in vivo ROS staining experiments demonstrated a significant increase in intratumoral oxidative stress in mice from both the SAM@BTO + US group and the VA-SAM@BTO + US group, as indicated by the intense red fluorescence emitted by the ROS probe. Furthermore, the hematoxylin and eosin (H&E) and terminal deoxynucleotidyl transferase-mediated deoxyuridine triphosphate nick end labeling (TUNEL) staining results provided additional confirmation of the

therapeutic efficacy of VA-SAM@BTO + US. In mice treated with VA-SAM@BTO + US, substantial shedding of tumor tissue was observed, and tumor cells exhibited widespread necrosis or apoptosis. Similarly, TUNEL staining revealed that the synergistic therapy guided by VA-SAM@BTO + US had the most potent induction effect on tumor cell apoptosis.

### Immunological effect of VA-SAM@BTO in vivo

Tumor cell metabolism is considered a crucial factor influencing the TME and posing challenges for various cancer therapies, particularly immunotherapy. We performed a targeted metabolomics study on treated tumors using liquid chromatography–tandem mass spectrometry. Notably, the VA-SAM@BTO + US group exhibited the highest LA consumption within the tumor and disrupted the tumor's tricarboxylic acid (TCA) cycle (Fig. 8A). The findings revealed that VA-SAM@BTO + US effectively induced metabolic disruption in situ CRC. In addition, we were delighted to discover that the metabolic disturbance resulting from VA-SAM@BTO + US treatment led to a significant reduction in the levels of three immunosuppressive metabolites (Fig. 8B).

We used flow cytometry to analyze the infiltration of immune cells orthotopically within CRC (Fig. 8C). Compared to mice treated with PBS, those treated with VA-SAM@BTO + US exhibited a significant decrease in the percentage of M2-like tumor-associated macrophages (TAMs) from 24.1 to 12.5% (Fig. 8D and figs. S27 and S28), while the percentage of M1-like TAMs increased significantly from 11.4 to 28.5% (Fig. 8, C and D). In addition, the treatment resulted in a substantial increase in mature DCs within the tumor tissue (Fig. 8E and fig. S29). Furthermore, following treatment with SAM@BTO + US, there was a moderate decrease in M2-like TAMs and a mild increase in M1-like TAMs and mature DCs, possibly attributable to the immunomodulatory effects of ROS or released CO generated by BTO. Moreover, we observed that VA treatment also had a positive impact on the M1 polarization of macrophages and maturation of DCs, indicating that the immunogenicity and LA metabolism of VA could also contribute to the reversal of the tumor immunosuppressive microenvironment.

Moreover, our in-depth analysis of T cell infiltration within the tumor revealed compelling results. As illustrated in Fig. 8 (F to H) and fig. S30, the combination treatment of VA-SAM@BTO + US demonstrated the lowest expression of  $T_{reg}$  cells and the highest expression of  $CD8^+$  T and  $CD4^+$  T cells, highly surpassing the effects of SAM@BTO + US and VA treatment. This suggests that LA consumption significantly inhibits the activity of  $T_{reg}$  and enhances the cytotoxic activity of T cells. In addition, the excessive production of ROS and CO also demonstrates remarkable local immune activation ability. Subsequently, we used enzyme-linked immunosorbent assay (ELISA) to assess various typical cytokines in the tumor tissue. These included interleukin-10 (IL-10) secreted by M2-like TAMs, myeloid-derived suppressor cells (MDSCs), and Tregs, as well as IL-1, IL-2, IL-3, IL-6, IL-12, and interferon-gamma (IFN- $\gamma$ ) secreted by  $CD8^+$  T cells. Our findings indicated that the tumor lysate supernatant of mice treated with VA-SAM@BTO exhibited the lowest level of IL-10 (Fig. 8I) while showing the highest levels of IL-6 (Fig. 8J) and IL-12 (Fig. 8K). These results confirm the polarization of TAMs from M2 to M1 mediated by ROS and CO, as well as the reduction in MDSCs and Tregs. Furthermore, the level of IFN- $\gamma$  in mice treated with VA-SAM@BTO was significantly increased by 3.8-fold compared to that in mice treated with PBS, providing further evidence of immune activation (Fig. 8L).

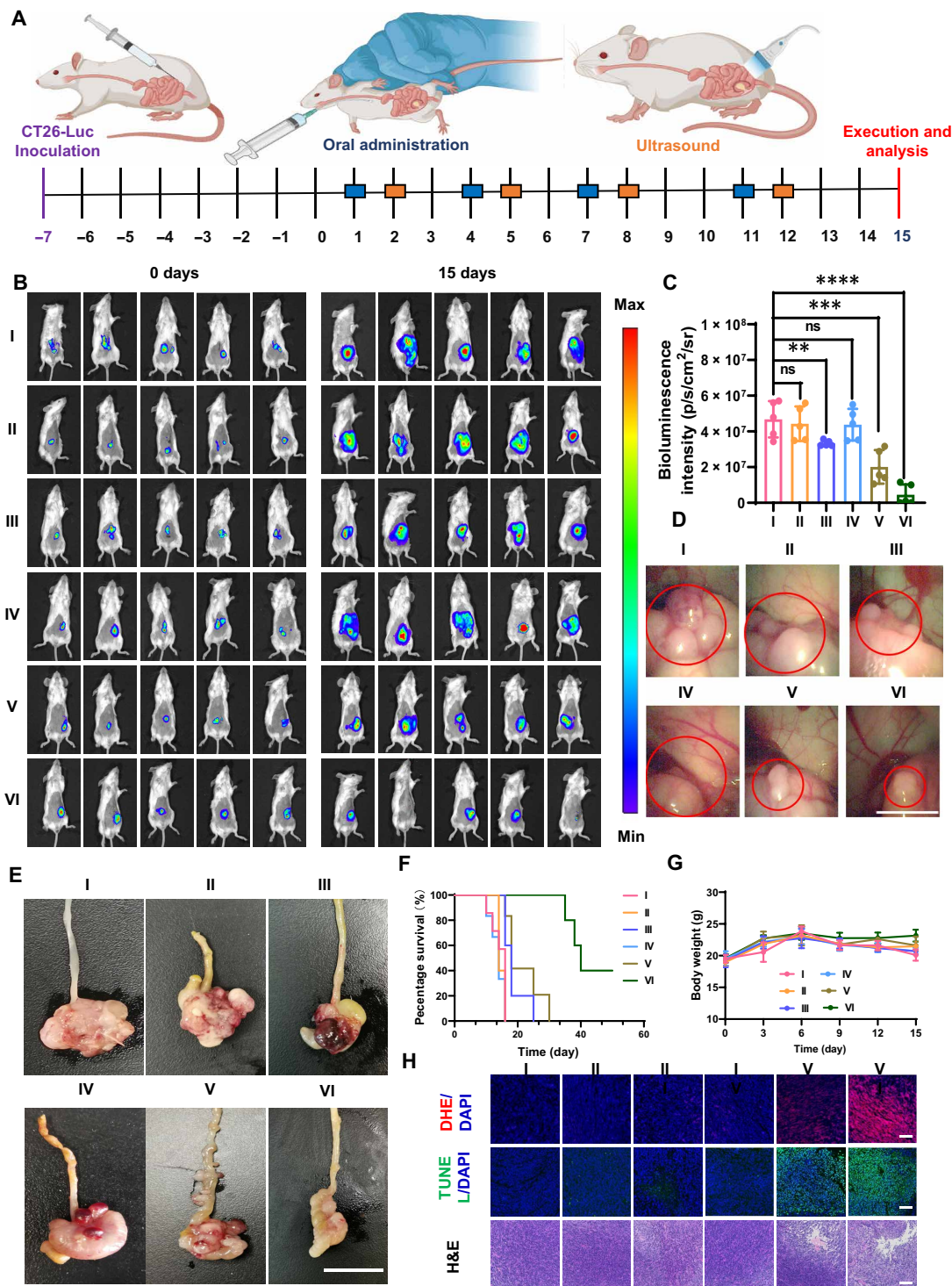


**Fig. 7. In vivo antitumor effect of VA-SAM@BTO upon US irradiation.** (A) Schematic showing the experimental process of VA-SAM@BTO in vivo antitumor therapy. (B) The IVIS images of the orthotopic CRC mice on day 0 and day 15. (C) The corresponding bioluminescence intensity of the orthotopic CRC mice on day 15. (D) Laparoscopic images of orthotopic CRC mice on day 10. Scale bar, 1 cm. (E) Photographs showing the antitumor performance of the orthotopic CRC mice. Scale bar, 1 cm. (F) The percentage survival and (G) body weight of the orthotopic CRC mice. All the results are presented as the means  $\pm$  SDs ( $n = 5$ ). (H) Dihydroethidium, TUNEL, and H&E staining of tumor tissues. Scale bars, 100  $\mu\text{m}$ . I: PBS, II: SAM@BTO, III: VA, IV: US, V: SAM@BTO + US, VI: VA-SAM@BTO + US. Statistical significance was determined using ANOVA followed by Tukey's multiple comparison test (\*\* $P < 0.01$ , \*\*\* $P < 0.001$ , and \*\*\*\* $P < 0.0001$ ).

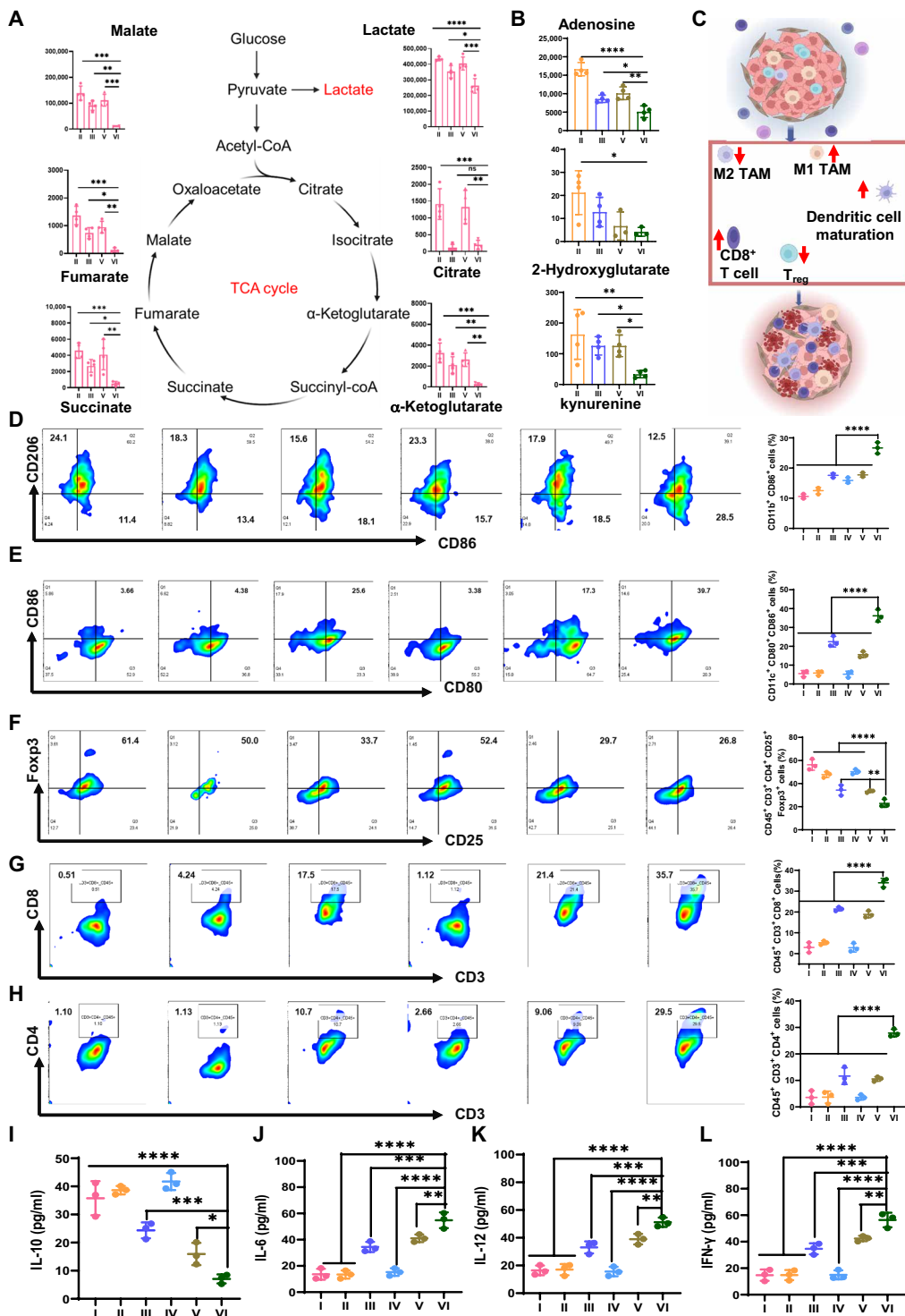


**Fig. 8. In vivo section staining and immunomodulation analysis.** (A) Intratumoral levels of TCA cycle metabolites measured by liquid chromatography–tandem mass spectrometry ( $n = 4$ ). (B) The intratumoral adenosine, 2-hydroxyglutarate, and kynurene content in CRC tumors after various treatments. (C) Schematic showing the mechanisms by which VA-SAM@BTO mediates the immunomodulatory effect of the TME in CRC. (D to H) Representative flow cytometry images and corresponding quantification of M1-like ( $CD11b^+CD86^+$ ), DC ( $CD11c^+CD80^+CD86^+$ ),  $T_{reg}$  ( $CD45^+CD3^+CD4^+CD25^+Foxp3^+$ ),  $CD8^+$  T cells ( $CD45^+CD3^+CD8^+$ ), and  $CD4^+$  T cells ( $CD45^+CD3^+CD4^+$ ) in tumor tissues. (I to L) Enzyme-linked immunosorbent assay analysis of orthotopic CRC mouse tissue. I: PBS, II: SAM@BTO, III: VA, IV: US, V: SAM@BTO + US, VI: VA-SAM@BTO + US. The data are presented as the means  $\pm$  SD. All the results are presented as the means  $\pm$  SDs ( $n = 3$ ). Statistical significance was determined using ANOVA followed by Tukey's multiple comparison test (\* $P < 0.05$ , \*\* $P < 0.01$ , \*\*\* $P < 0.001$ , and \*\*\*\* $P < 0.0001$ ).

In summary, on the basis of intratumoral metabolomics analysis and the immunological effect of VA-SAM@BTO in vivo, we found a positive correlation between LA levels and tumor immunosuppression in the different treatment groups. The VA-SAM@BTO + US group exhibited the highest LA consumption within the tumor and disrupted the tumor's TCA cycle resulting in metabolic disturbance. This treatment approach achieved the most potent immune activation effect. Catalytic synergistic immunotherapy mediated by VA-SAM@BTO + US effectively transforms “cold” CRC cells into a “hot” TME, indicating the establishment of an immune-functional TME conducive to immunotherapy.

### The abundance of gut microbiota

Multiple studies have demonstrated that tumor progression can affect the composition of the gut microbiota, and, in turn, the gut microbiota can shape the TME, thus influencing the antitumor immune response (53, 54). Through an analysis of the fecal microbiota of treated mice and healthy mice, we confirmed the regulatory effect of VA-SAM@BTO + US treatment on the gut microbiota. As shown in Fig. 9A, the mice with *in situ* CRC treated with VA-SAM@BTO + US and the healthy group of mice exhibited a similar composition of gut microbiota. On the basis of the 16S rDNA identification presented in Fig. 9 (B and C), significant changes were observed in mice treated with VA-SAM@BTO + US compared to the control group, as indicated by distinct clustering patterns in the nonmetric multidimensional scaling analysis of beta diversity. At the family level, the abundance of Lachnospiraceae, Rikenellaceae, Bacteroidaceae, Ruminococcaceae, Tannerellaceae, and Akkermansiaceae was notably increased in the VA-SAM@BTO + US treatment group (Fig. 9D). Furthermore, at the genus level, the abundance of Roseburia decreased in the control group but increased in the VA-SAM@BTO + US group (Fig. 9E). In addition, as depicted in Fig. 9F, the abundance of beneficial bacterial genera, such as Lachnospiraceae, Roseburia, Akkermansia, Tannerellaceae, Clostridia, and Ruminococcaceae, which are known to produce SCFAs, significantly increased after VA-SAM@BTO + US treatment. SCFAs are well-established biomarkers for predicting the progression of CRC and serve as therapeutic targets for delaying or preventing CRC progression. Hence, we further examined the impact of VA-SAM@BTO + US on SCFAs. As shown in Fig. 9 (G and H), we were pleasantly surprised to find that there was a remarkable increase in SCFA production in the orthotopic CRC mouse group following VA-SAM@BTO + US treatment compared to that in the control group. These results suggest that VA-SAM@BTO + US may alter the gut microenvironment and impede disease progression by restoring the abundance of the gut microbiota, increasing the proportion of beneficial bacteria, and elevating SCFA levels.

### Biosafety evaluation of VA-SAM@BTO

To further validate the biocompatibility and specific targeted antitumor mechanism of VA-SAM@BTO-based therapies, we conducted a thorough investigation of the biosafety of VA-SAM@BTO through histological examination, routine blood examination, and blood biochemical analyses. As depicted in Fig. 10A, minimal inflammatory damage was observed in the tissue sections of each group of agents. Furthermore, real-time quantitative polymerase chain reaction was used to assess the damage and inflammatory response of major organs exposed to each group of agents. The results displayed in Fig. 10B indicate that there was no significant inflammatory

response for all groups of agents, thereby confirming the biosafety of VA-SAM@BTO + US-based cancer therapies.

To delve deeper, we also assessed the impact of orally administered VA-SAM@BTO on the blood routine of healthy mice after 7 and 14 days. The routine blood indexes, including MCHC, RBC, HCT, WBC, PLT, MCV, HGB, and MCH, showed no statistically significant difference in the VA-SAM@BTO-treated group compared to the PBS group. In addition, the blood biochemical indices, as shown in Fig. 10D, displayed little observable difference between the PBS control mice and those orally administered VA-SAM@BTO for 1, 7, and 14 days. As shown in fig. S31, 2 weeks after oral administration of VA-SAM@BTO, no significant organ damage was observed in the major tissues of the organisms. Moreover, we further investigated the biodistribution and metabolic elimination of VA-SAM@BTO nanomaterials by using inductively coupled plasma mass spectrometry (fig. S32). The results showed that the Ba concentration in the tumor site significantly increased after oral administration, demonstrating that VA-SAM@BTO was enriched at the tumor sites. In addition, the metabolites of nanoparticles and long-term biosafety are highly important. Therefore, we further detected the Ba content 15 and 30 days after treatment. At 30 days after treatment, the Ba content in the main tissues decreased to a very low level compared with that on the first day after treatment, which indicated that most VA-SAM@BTO was metabolized and excreted from the body. These findings collectively indicate that the prepared VA-SAM@BTO material exhibits excellent biocompatibility and biosafety.

### DISCUSSION

In this study, we developed a clever strategy using microrobots for treating tumors by using the unique physiological structure and metabolic characteristics of VA. We started by synthesizing tetravalent piezoelectric ceramic material BTO nanocubes through a hydrothermal method. To enhance their functionality, we coated the nanocubes with an *S. aureus* membrane (SAM@BTO). This coating not only allowed for active targeting of tumors but also provided a reactive site for modifying the BTO elements on the VA surface. Through a classic click chemical reaction, we encapsulated SAM@BTO on the surface of VA cells, creating VA-SAM@BTO. By combining the inflammatory targeting of SAM and the anaerobic targeting of VA cells, we built a multidirectional collaborative treatment platform for tumors. This system effectively achieves tumor double targeting and enables deep tumor penetration. When orally administered, this treatment platform accurately targets *in situ* CRC and is capable of long-lasting retention and tumor penetration. Under *in vitro* US stimulation, BTO exhibits an efficient piezoelectric effect, enabling it to catalyze two reduction reactions ( $O_2 \rightarrow \cdot O_2^-$  and  $CO_2 \rightarrow CO$ ) and three oxidation reactions ( $H_2O \rightarrow \cdot OH$ ,  $GSH \rightarrow GSSG$ , and  $LA \rightarrow PA$ ) simultaneously. This leads to the proliferation of ROS and CO, which synergistically induce immunogenic cell death in tumor cells and activate the immune response. BTO also catalyzes the LA oxidation coupling of LA consumption by VA cells, effectively disrupting the immunosuppressive microenvironment caused by high LA levels. Consequently, it enhances DC cell maturation and macrophage M1 polarization, increases the proportion of effector T cells, and decreases the number of  $T_{reg}$  cells. Furthermore, the biological hybrid robots demonstrated excellent biosafety both *in vitro* and *in vivo*, indicating their potential for practical

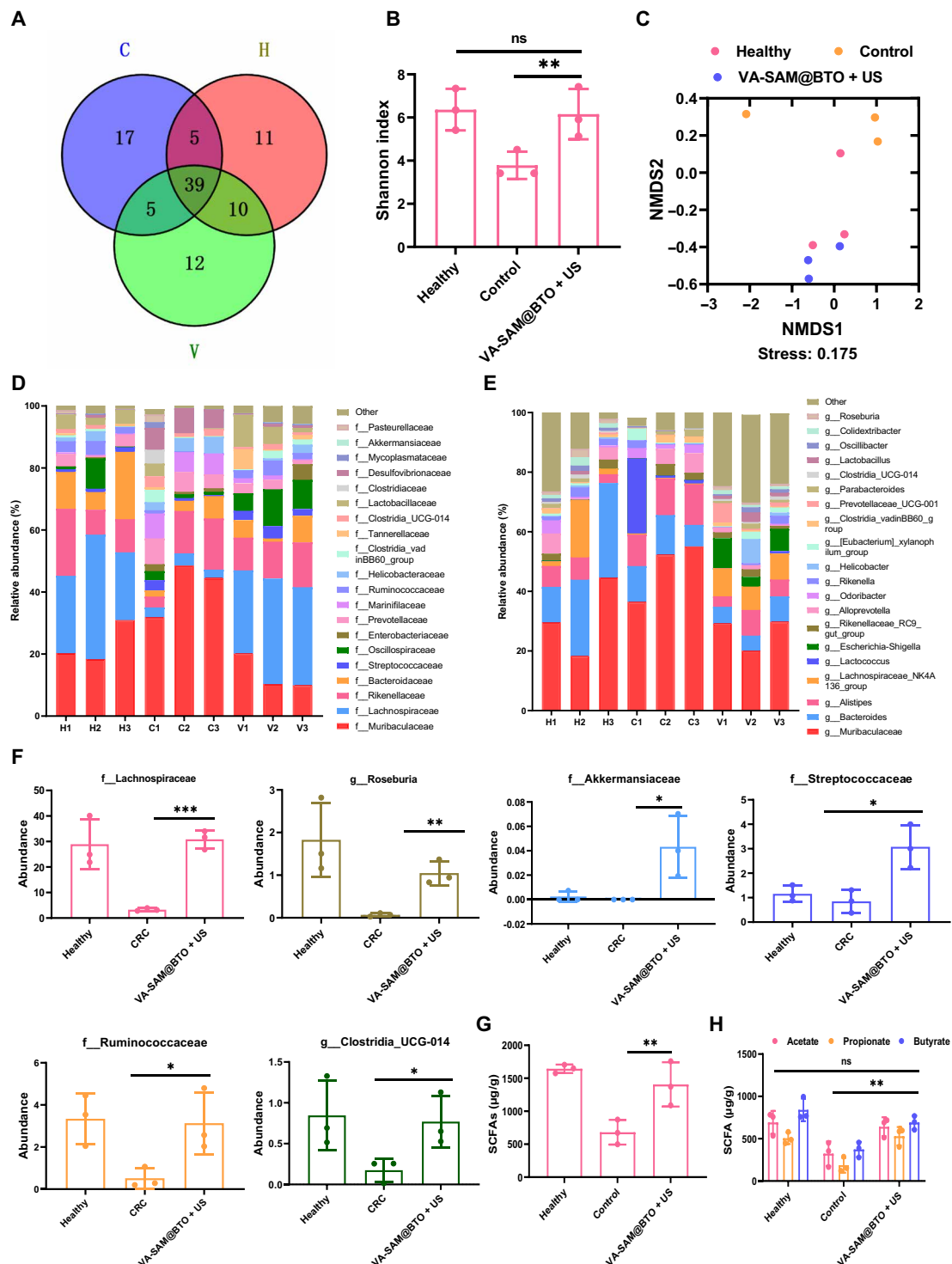


**Fig. 9. The modulation of intestinal microbiota by VA-SAM@BTO.** (A) Venn diagram of identified bacterial strains in the feces of healthy group mice, as well as in the fecal samples of the control group and VA-SAM@BTO + US-treated *in situ* CRC mice. (B) Microbial  $\alpha$  diversity at the amplicon sequence variant (ASV) level was evaluated using the Shannon index. (C) The microbial  $\beta$  diversity at the ASV level, based on the Bray-Curtis distance, was analyzed via nonmetric multidimensional scaling (NMDS). The relative abundance of intestinal microbial families at the family level (D) and the genus level (E). (F) The relative abundances of Lachnospiraceae, Roseburia, Akkermansiaeae, Tannerellsceae, Clostridia, and Ruminococcaceae in each group. (G) A summary of SCFA and (H) acetate, propionate, and butyrate levels in the different groups. The data are presented as the means  $\pm$  SD ( $n = 3$  mice). Statistical significance was determined using one-way ANOVA combined with Tukey's post hoc test (\* $P < 0.05$ , \*\* $P < 0.01$ , and \*\*\* $P < 0.001$ ).

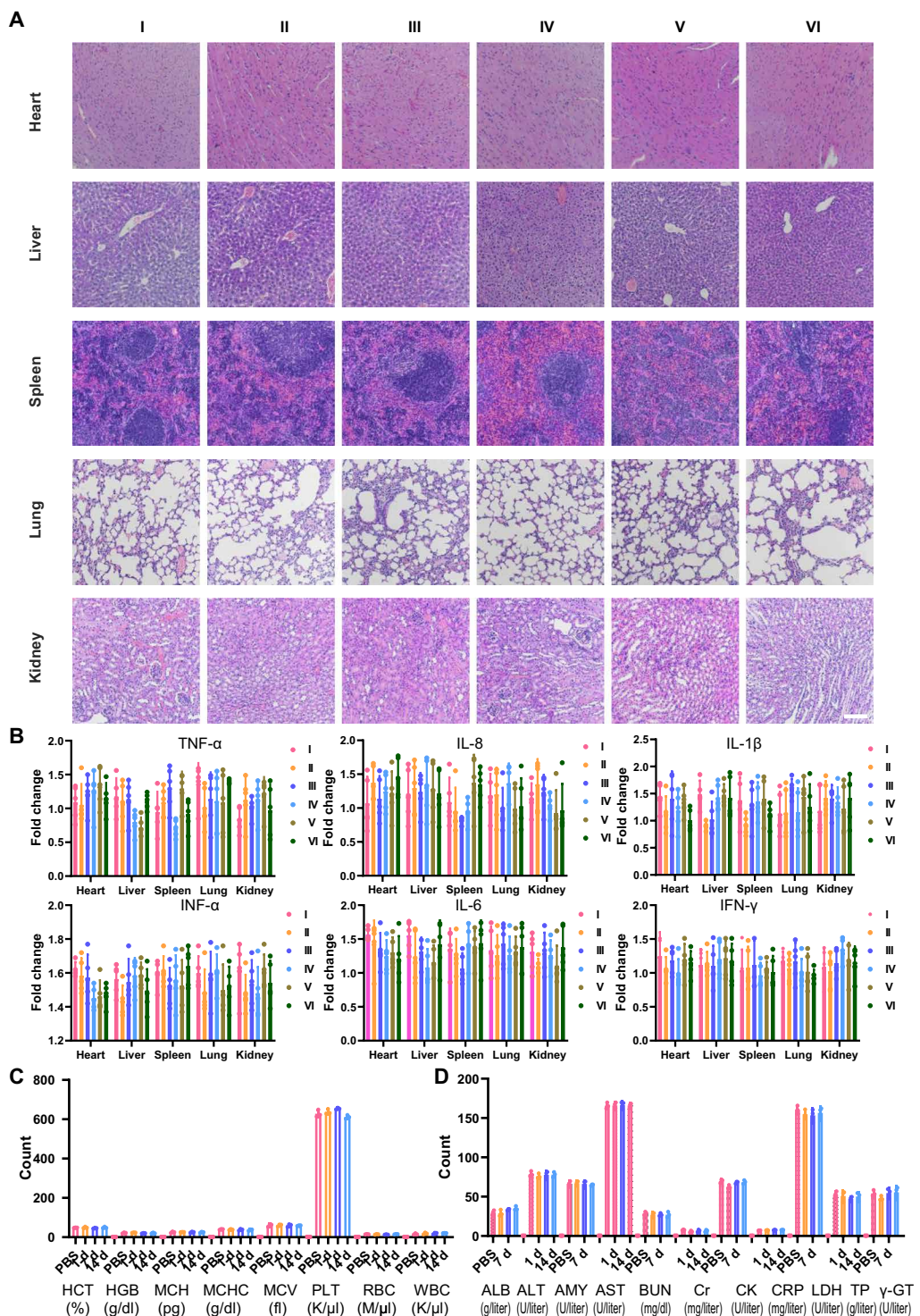


**Fig. 10. Biosafety evaluation of VA-SAM@BTO.** (A) Representative H&E-stained images of major organs. Scale bar, 100  $\mu$ m. (B) ELISA analysis of mouse data ( $n = 5$  biologically independent mice). (C) Routine blood analysis of the mice. (D) Biochemical analysis of BALB/c mice is shown as the means  $\pm$  SD ( $n = 5$  biologically independent mice). I: PBS, II: SAM@BTO, III: VA, IV: US, V: SAM@BTO + US, VI: VA-SAM@BTO + US.

application and clinical translation. Overall, our study highlights the effectiveness and safety of the developed biological hybrid robots for targeted antitumor therapy, providing a promising approach for future therapeutic interventions.

Most of the biohybrid tumor treatment systems previously reported based on active microorganisms use microorganisms as simple delivery carriers, and there is no synergy between the microbial system and the loaded nanomedicine. In addition, some studies involve the use of genetically engineered microorganisms for therapeutic purposes other than delivery, which also increases the complexity and instability of biohybrid nanomedicine preparations. In this study, VA, which is naturally consumed by LA, was used as a carrier to load SAM-coated BTO to achieve synergistic catalytic and immune treatment of CRC. The main innovations and advantages of these methods are mainly reflected in the following aspects. First, the preparation method of biohybrid systems is simple, and the process is mature. Second, SAM and VA were used to achieve cascade targeting of the formulation, which increased its bioavailability. Third, in vitro US stimulation can not only mediate efficient targeted catalytic therapy for tumors but also enhance the ability of VA to consume LA through the oxidation of separated holes, reflecting a good synergistic effect between nanomedicine and microbial carriers. Last, the strategy reported in this study mediates highly effective synergistic tumor catalysis and immune therapy through the effective killing of the primary tumor and regulation of the immunosuppressive microenvironment.

Despite the promising results shown in preclinical studies, bionanomaterial-functionalized bacterial therapies may exhibit significant differences in behavior and efficacy within the complex physiological environment of a living organism. Factors such as immune reactions, clearance mechanisms, and biofilm formation can affect the therapeutic effectiveness and overall success rate of bacterial therapies. Therefore, additional comprehensive *in vivo* research is needed to determine the effectiveness of bacterial therapeutic formulations. In terms of clinical translation, scalability and reproducibility issues concerning bionanomaterial-functionalized bacterial therapies also need to be addressed. Manufacturing large quantities of consistent and high-quality bionanomaterial-functionalized bacterial therapies may be challenging. In conclusion, robust production methods for bionanomaterial-functionalized bacteria that can meet clinical demands while maintaining therapeutic efficacy are urgently needed.

## MATERIALS AND METHODS

### Preparation of VA-SAM@BTO

After the initial washing of VA bacterial cells with Mops buffer to remove any residual RCM medium and subsequent suspension in Mops buffer, approximately  $1 \times 10^8$  VA bacterial cells were subjected to treatment with 30  $\mu\text{M}$  azido-PEG4-NHS ester at room temperature for a duration of 1 hour. Next, SAM@BTO nanoparticles were exposed to 50  $\mu\text{M}$  DBCO-PEG4-NHS ester at room temperature for 1 hour to undergo modification with azide groups for the purpose of click chemistry. The VA cells and SAM@BTO nanoparticles were then separately washed three times with Mops buffer to eliminate any unreacted NHS ester, thereby preparing them for subsequent covalent binding. To optimize the binding efficiency, various concentrations of nanoparticles (0.05, 0.1, 0.2, and 0.5 mg/ml) were used for covalent binding. During the covalent binding process, DBCO-modified

nano particles were coincubated with azide-functionalized VA cells for a period of 45 min. Subsequently, the resultant VA-SAM@BTO covalent conjugate was collected following centrifugation at 7000g for 5 min and underwent a further three washes with Mops buffer in preparation for subsequent characterization.

### Intracellular cytotoxicity assay of VA-SAM@BTO

Mouse CRC cells (CT26, catalog number: CRL-2638) and CT26 cells transfected with luciferase (CT26-luc) were obtained from the American Type Culture Collections. CT26 cells were seeded in the bottom chamber of a 24-well transwell at a density of  $5 \times 10^4$  cells per well and cultured in RPMI 1640 medium (0.5 ml per well) containing 10% fetal bovine serum for 12 hours. Subsequently, different materials (SAM@BTO, VA, US, SAM@BTO + US, VA-SAM@BTO + US) were added to the top chamber of the transwell and coincubated with CT26 cells for 12 hours. The cells were then irradiated with US and US treatment (1 MHz, 1 W cm<sup>-2</sup>, 50% duty cycle), followed by further incubation for 12 hours. For the *in vitro* cytotoxicity assay, CCK-8 solution (100  $\mu\text{l}$ , 10% CCK-8) was added, and the cells were further incubated for 1 hour. The absorbance of each well at 450 nm was then measured using a microplate reader.

### Establishment of orthotopic colorectal cancer animal model

All animal experiments were approved by the Animal Ethics Committee of the Tianjin University Laboratory Animal Center and conducted in accordance with the Guidelines for the Care and Use of Laboratory Animals of Tianjin University. The approved animal experiment number is TJUE-2023-253. In the orthotopic CRC model, luciferase-transfected CT26 cells ( $2 \times 10^6$  cells per mouse) were implanted in the cecum of female BALB/c mice (8 weeks, 20 to 22 g). Tumor growth was monitored using the IVIS (PerkinElmer) system for bioluminescence imaging. Following the same procedure,  $2 \times 10^6$  MC38 cells were intraperitoneally injected into each BALB/c mouse to establish the MC38 tumor mouse model.

### Antitumor therapy *in vivo*

In the orthotopic CRC model, mice with tumors were randomly assigned to six groups ( $n = 5$  per group): (i) PBS, (ii) SAM@BTO, (iii) VA, (iv) US, (v) SAM@BTO + US, and (vi) VA-SAM@BTO + US. The final concentration of VA was  $1 \times 10^8$  CFU per mouse, and the final concentration of BTO was 10 mg/kg. The US treatment conditions were set at a 1 MHz frequency, 1 W cm<sup>-2</sup> intensity, 50% duty cycle, and 5-min duration. The growth of the orthotopic tumors was monitored through bioluminescence imaging using an IVIS system from PerkinElmer. After undergoing various treatments, the mice were euthanized and dissected to assess disease progression. Several major organs were collected and preserved in 4% paraformaldehyde for histological analysis. Furthermore, the body weights of the mice were monitored every 3 days.

## Supplementary Materials

**This PDF file includes:**

Supplementary Text  
Figs. S1 to S32

## REFERENCES AND NOTES

- K. E. de Visser, J. A. Joyce, The evolving tumor microenvironment: From cancer initiation to metastatic outgrowth. *Cancer Cell* **41**, 374–403 (2023).

2. G. Bergers, S.-M. Fendt, The metabolism of cancer cells during metastasis. *Nat. Rev. Cancer* **21**, 162–180 (2021).
3. I. Martinez-Reyes, N. S. Chandel, Cancer metabolism: Looking forward. *Nat. Rev. Cancer* **21**, 669–680 (2021).
4. S. Hui, J. M. Ghergurovich, R. J. Morscher, C. Jang, X. Teng, W. Lu, L. A. Esparza, T. Reya, Z. Le, J. Yanxiang Guo, E. White, J. D. Rabinowitz, Glucose feeds the TCA cycle via circulating lactate. *Nature* **551**, 115–118 (2017).
5. C. Heuser, K. Renner, M. Kreutz, L. Gattinoni, Targeting lactate metabolism for cancer immunotherapy - a matter of precision. *Semin. Cancer Biol.* **88**, 32–45 (2023).
6. Y. Qian, A. Galan-Cobo, I. Guijarro, M. Dang, D. Molkentine, A. Poteete, F. Zhang, Q. Wang, J. Wang, E. Parra, A. Panda, J. Fang, F. Skoulidis, I. I. Wistuba, S. Verma, T. Merghoub, J. D. Wolchok, K. K. Wong, R. J. DeBerardinis, J. D. Minna, N. I. Vokes, C. B. Meador, J. F. Gainor, L. Wang, A. Reuben, J. V. Heymach, MCT4-dependent lactate secretion suppresses antitumor immunity in LKB1-deficient lung adenocarcinoma. *Cancer Cell* **41**, 1363–1380.e7 (2023).
7. L. Ippolito, A. Morandi, E. Giannoni, P. Chiarugi, Lactate: A metabolic driver in the tumour landscape. *Trends Biochem. Sci.* **44**, 153–166 (2019).
8. Z. Cao, D. Xu, J. Harding, W. Chen, X. Liu, Z. Wang, L. Wang, T. Qi, S. Chen, X. Guo, I. S. Y. Chen, J. Guo, Y. Lu, J. Wen, Lactate oxidase nanocapsules boost T cell immunity and efficacy of cancer immunotherapy. *Sci. Transl. Med.* **15**, eadd2712 (2023).
9. M. Certo, C. H. Tsai, V. Pucino, P. C. Ho, C. Mauro, Lactate modulation of immune responses in inflammatory versus tumour microenvironments. *Nat. Rev. Immunol.* **21**, 151–161 (2021).
10. M. J. Watson, P. D. A. Vignali, S. J. Mullett, A. E. Overacre-Delgoffe, R. M. Peralta, S. Grebiniski, A. V. Menk, N. L. Rittenhouse, K. DePeaux, R. D. Whetstone, D. A. A. Vignali, T. W. Hand, A. C. Poholek, B. M. Morrison, J. D. Rothstein, S. G. Wendell, G. M. Delgoffe, Metabolic support of tumour-infiltrating regulatory T cells by lactic acid. *Nature* **591**, 645–651 (2021).
11. J. A. Bluestone, Q. Tang,  $T_{reg}$  cells—The next frontier of cell therapy. *Science* **362**, 154–155 (2018).
12. R. Zappasodi, I. Serganova, I. J. Cohen, M. Maeda, M. Shindo, Y. Senbabaoglu, M. J. Watson, A. Leftin, R. Maniyar, S. Verma, M. Lubin, M. Ko, M. M. Mane, H. Zhong, C. Liu, A. Ghosh, M. Abu-Akeel, E. Ackerstaff, J. A. Koutcher, P.-C. Ho, G. M. Delgoffe, R. Blasberg, J. D. Wolchok, T. Merghoub, CTLA-4 blockade drives loss of  $T_{reg}$  stability in glycolysis-low tumours. *Nature* **591**, 652–658 (2021).
13. A. Tasdogan, B. Faubert, V. Ramesh, J. M. Ubellacker, B. Shen, A. Solmonson, M. M. Murphy, Z. Gu, W. Gu, M. Martin, S. Y. Kasititon, T. Vandergriff, T. P. Mathews, Z. Zhao, D. Schadendorf, R. J. DeBerardinis, S. J. Morrison, Metabolic heterogeneity confers differences in melanoma metastatic potential. *Nature* **577**, 115–120 (2020).
14. T. P. Brown, V. Ganapathy, Lactate/GPR81 signaling and proton motive force in cancer: Role in angiogenesis, immune escape, nutrition, and warburg phenomenon. *Pharmacol. Ther.* **206**, 107451 (2020).
15. J. Xiong, J. He, J. Zhu, J. Pan, W. Liao, H. Ye, H. Wang, Y. Song, Y. Du, B. Cui, M. Xue, W. Zheng, X. Kong, K. Jiang, K. Ding, L. Lai, Q. Wang, Lactylation-driven METTL3-mediated RNA m<sup>6</sup>A modification promotes immunosuppression of tumor-infiltrating myeloid cells. *Mol. Cell* **82**, 1660–1677.e10 (2022).
16. J. E. Bader, K. Voss, J. C. Rathmell, Targeting metabolism to improve the tumor microenvironment for cancer immunotherapy. *Mol. Cell* **78**, 1019–1033 (2020).
17. R. G. Feichtinger, R. Lang, Targeting L-Lactate metabolism to overcome resistance to immune therapy of melanoma and other tumor entities. *J. Oncol.* **2019**, 2084195 (2019).
18. J. Chen, Y. Zhu, C. Wu, J. Shi, Engineering lactate-modulating nanomedicines for cancer therapy. *Chem. Soc. Rev.* **52**, 973–1000 (2023).
19. S. V. Rajagopala, S. Vashee, L. M. Oldfield, Y. Suzuki, J. C. Venter, A. Telenti, K. E. Nelson, The human microbiome and cancer. *Cancer Prev. Res.* **10**, 226–234 (2017).
20. E. Riquelme, Y. Zhang, L. Zhang, M. Montiel, M. Zoltan, W. Dong, P. Quesada, I. Sahin, V. Chandra, A. San Lucas, P. Scheet, H. Xu, S. M. Hanash, L. Feng, J. K. Burks, K. A. Do, C. B. Peterson, D. Nejman, C. D. Tzeng, M. P. Kim, C. L. Sears, N. Ajami, J. Petrosino, L. D. Wood, A. Maitra, R. Straussman, M. Katz, J. R. White, R. Jenq, J. Wargo, F. McAllister, Tumor microbiome diversity and composition influence pancreatic cancer outcomes. *Cell* **178**, 795–806 (2019).
21. E. M. Park, M. Chelvanambi, N. Bhutiani, G. Kroemer, L. Zitzvogel, J. A. Wargo, Targeting the gut and tumor microbiota in cancer. *Nat. Med.* **28**, 690–703 (2022).
22. J. Svensson-Arvelund, S. Cuadrado-Castano, G. Pantulaia, K. Kim, M. Aleynick, L. Hamerich, R. Upadhyay, M. Yellin, H. Marsh, D. Orepel, S. Jhunjhunwala, C. Moussion, M. Merad, B. D. Brown, A. Garcia-Sastre, J. D. Brody, Expanding cross-presenting dendritic cells enhances oncolytic virotherapy and is critical for long-term anti-tumor immunity. *Nat. Commun.* **13**, 7149 (2022).
23. M. M. Rahman, G. McFadden, Oncolytic viruses: Newest frontier for cancer immunotherapy. *Cancer* **13**, 5452 (2021).
24. A. T. Crespo, S. Burnell, L. Capitaní, R. Bayliss, E. Moses, G. H. Mason, J. A. Davies, A. J. Godkin, A. M. Gallimore, A. L. Parker, Pouring petrol on the flames: Using oncolytic virotherapies to enhance tumour immunogenicity. *Immunology* **163**, 389–398 (2021).
25. S. Z. Shalhout, D. M. Miller, K. S. Emerick, H. L. Kaufman, Therapy with oncolytic viruses: Progress and challenges. *Nat. Rev. Clin. Oncol.* **20**, 160–177 (2023).
26. C. R. Gurbatri, N. Arpaia, T. Danino, Engineering bacteria as interactive cancer therapies. *Science* **378**, 858–864 (2022).
27. Q. W. Chen, J. Y. Qiao, X. H. Liu, C. Zhang, X. Z. Zhang, Customized materials-assisted microorganisms in tumor therapeutics. *Chem. Soc. Rev.* **50**, 12576–12615 (2021).
28. X. Ma, X. Liang, Y. Li, Q. Feng, K. Cheng, N. Ma, F. Zhu, X. Guo, Y. Yue, G. Liu, T. Zhang, J. Liang, L. Ren, X. Zhao, G. Nie, Modular-designed engineered bacteria for precision tumor immunotherapy via spatiotemporal manipulation by magnetic field. *Nat. Commun.* **14**, 1606 (2023).
29. J. X. Fan, M. T. Niu, Y. T. Qin, Y. X. Sun, X. Z. Zhang, Progress of engineered bacteria for tumor therapy. *Adv. Drug Deliv. Rev.* **185**, 114296 (2022).
30. Y. E. Chen, D. Bousbaine, A. Veinbachs, K. Atabakhsh, A. Dimas, V. K. Yu, A. Zhao, N. J. Enright, K. Nagashima, Y. Belkaid, M. A. Fischbach, Engineered skin bacteria induce antitumor T cell responses against melanoma. *Science* **380**, 203–210 (2023).
31. J. Scheiman, J. M. Luber, T. A. Chavkin, T. MacDonald, A. Tung, L. D. Pham, M. C. Wibowo, R. C. Wurth, S. Punthambaker, B. T. Tierney, Z. Yang, M. W. Hattab, J. Avila-Pacheco, C. B. Clish, S. Lessard, G. M. Church, A. D. Kostic, Meta-omics analysis of elite athletes identifies a performance-enhancing microbe that functions via lactate metabolism. *Nat. Med.* **25**, 1104–1109 (2019).
32. L. Rong, Q. Lei, X. Z. Zhang, Engineering living bacteria for cancer therapy. *ACS Appl. Bio Mater.* **3**, 8136–8145 (2020).
33. Z. Wang, M. Chu, N. Yin, W. Huang, W. Liu, Z. Zhang, J. Liu, J. Shi, Biological chemotaxis-guided self-thermophoretic nanoplatform augments colorectal cancer therapy through autonomous mucus penetration. *Sci. Adv.* **8**, eabn3917 (2022).
34. Y. Zhang, C. Li, X. Zhang, Bacteriophage-mediated modulation of microbiota for diseases treatment. *Adv. Drug Deliv. Rev.* **176**, 113856 (2021).
35. Y. Chen, Z. Li, X. Zeng, X. Zhang, Bacteria-based bioactive materials for cancer imaging and therapy. *Adv. Drug Deliv. Rev.* **193**, 114696 (2023).
36. R. Su, H. A. Hsain, M. Wu, D. Zhang, X. Hu, Z. Wang, X. Wang, F. Li, X. Chen, L. Zhu, Y. Yang, Y. Yang, X. Lou, S. J. Pennycook, Nano-ferroelectric for high efficiency overall water splitting under ultrasonic vibration. *Angew. Chem. Int. Ed. Engl.* **58**, 15076–15081 (2019).
37. Z. Wang, W. Huang, S. Zhang, M. Chu, N. Yin, C. Zhu, Z. Zhang, J. Shi, J. Liu, Self-thermophoretic nanoparticles enhance intestinal mucus penetration and reduce pathogenic bacteria interception in colorectal cancer. *Adv. Funct. Mater.* **33**, 2212013 (2023).
38. S. Depienne, M. Bouzelha, E. Courtois, K. Pavageau, P. A. Lalys, M. Marchand, D. Alvarez-Dorta, S. Nedellec, L. Marín-Fernández, C. Grandjean, M. Boujittia, D. Deniaud, M. Mével, S. G. Gouin, Click-electrochemistry for the rapid labeling of virus, bacteria and cell surfaces. *Nat. Commun.* **14**, 5122 (2023).
39. F. Zhang, J. Zhuang, Z. Li, H. Gong, B. E. de Avila, Y. Duan, Q. Zhang, J. Zhou, L. Yin, E. Karshlev, W. Gao, V. Nizet, R. H. Fang, L. Zhang, J. Wang, Nanoparticle-modified microrobots for in vivo antibiotic delivery to treat acute bacterial pneumonia. *Nat. Mater.* **21**, 1324–1332 (2022).
40. S. Li, W. Jiang, C. Zheng, D. Shao, Y. Liu, S. Huang, J. Han, J. Ding, Y. Tao, M. Li, Oral delivery of bacteria: Basic principles and biomedical applications. *J. Control. Release* **327**, 801–833 (2020).
41. F. Cao, L. Jin, Y. Gao, Y. Ding, H. Wen, Z. Qian, C. Zhang, L. Hong, H. Yang, J. Zhang, Z. Tong, W. Wang, X. Chen, Z. Mao, Artificial-enzymes-armed bifidobacterium longum probiotics for alleviating intestinal inflammation and microbiota dysbiosis. *Nat. Nanotechnol.* **18**, 617–627 (2023).
42. X. Zhang, G. Chen, H. Zhang, L. Shang, Y. Zhao, Bioinspired oral delivery devices. *Nat. Biomed. Eng.* **1**, 208–225 (2023).
43. L. Chen, Z. Mao, Y. Wang, Y. Kang, Y. Wang, L. Mei, X. Ji, Edge modification facilitated heterogenization and exfoliation of two-dimensional nanomaterials for cancer catalytic therapy. *Sci. Adv.* **8**, eabo7372 (2022).
44. C. Yang, M. Wang, M. Chang, M. Yuan, W. Zhang, J. Tan, B. Ding, P. Ma, J. Lin, Heterostructural nanoaddjuvant CuSe/CoSe2for potentiating ferroptosis and photothermal immunotherapy through intratumoral blocked lactate efflux. *J. Am. Chem. Soc.* **145**, 7205–7217 (2023).
45. X. Yuan, Y. Kang, J. Dong, R. Li, J. Ye, Y. Fan, J. Han, J. Yu, G. Ni, X. Ji, D. Ming, Self-triggered thermoelectric nanoheterojunction for cancer catalytic and immunotherapy. *Nat. Commun.* **14**, 5140 (2023).
46. Y. Li, J. Dang, Q. Liang, L. Yin, Carbon monoxide (CO)-strengthened cooperative bioreductive anti-tumor therapy via mitochondrial exhaustion and hypoxia induction. *Biomaterials* **209**, 138–151 (2019).
47. Q. Tang, S. Sun, P. Wang, L. Sun, Y. Wang, L. Zhang, M. Xu, J. Chen, R. Wu, J. Zhang, M. Gong, Q. Chen, X. Liang, Genetically engineering cell membrane-coated bto nanoparticles for MMP2-activated piezocatalysis-immunotherapy. *Adv. Mater.* **35**, e2300964 (2023).

48. M. M. Azevedo, C. Pina-Vaz, F. Baltazar, Microbes and cancer: Friends or faux? *Int. J. Mol. Sci.* **21**, 3115 (2020).
49. Y. Xie, F. Xie, X. Zhou, L. Zhang, B. Yang, J. Huang, F. Wang, H. Yan, L. Zeng, L. Zhang, F. Zhou, Microbiota in tumors: From understanding to application. *Adv. Sci.* **9**, e2200470 (2022).
50. L. Zhao, J. Mei, G. Yu, L. Lei, W. Zhang, K. Liu, X. Chen, D. Kolat, K. Yang, J. K. Hu, Role of the gut microbiota in anticancer therapy: From molecular mechanisms to clinical applications. *Signal Transduct. Target. Ther.* **8**, 201 (2023).
51. D. Zheng, R. Li, J. An, T. Xie, Z. Han, R. Xu, Y. Fang, X. Zhang, Prebiotics-encapsulated probiotic spores regulate gut microbiota and suppress colon cancer. *Adv. Mater.* **32**, e2004529 (2020).
52. C. L. Ho, H. Q. Tan, K. J. Chua, A. Kang, K. H. Lim, K. L. Ling, W. S. Yew, Y. S. Lee, J. P. Thierry, M. W. Chang, Engineered commensal microbes for diet-mediated colorectal-cancer chemoprevention. *Nat. Biomed. Eng.* **2**, 27–37 (2018).
53. T. Lang, R. Zhu, X. Zhu, W. Yan, Y. Li, Y. Zhai, T. Wu, X. Huang, Q. Yin, Y. Li, Combining gut microbiota modulation and chemotherapy by capecitabine-loaded prebiotic nanoparticle improves colorectal cancer therapy. *Nat. Commun.* **14**, 4746 (2023).
54. S. Wong, J. Yu, Gut microbiota in colorectal cancer: Mechanisms of action and clinical applications. *Nat. Rev. Gastroenterol. Hepatol.* **16**, 690–704 (2019).

**Acknowledgments**

**Funding:** This study was financially supported by grants from the National Natural Science Foundation of China (grant no. 32071322, recipient: X.J.), National Natural Science Funds for Excellent Young Scholars (grant no. 32122044, recipient: X.J.), Technology & Innovation Commission of Shenzhen Municipality (grant no. JCYJ202103113004010, recipient: X.J.), the China Postdoctoral Science Foundation (grant nos. 2023 T160479 and 2023 M742603, recipient: Y.K.), and the Tianjin University 2023 Independent Innovation Fund Program (2023XQM-0043, recipient: Y.K.). **Author contributions:** Conceptualization: Y.F., J.Y., and X.J. Data curation: Y.F., J.Y., and Y.K. Formal analysis: Y.F., J.Y., and Y.K. Investigation: Y.F., J.Y., G.N., and J.S. Methodology: Y.F., J.Y., X.Y., R.L., and J.H. Project administration: Y.F. and X.J. Writing—original draft: Y.F. and X.J. Writing—review and editing: Y.F. and X.J. Funding acquisition: X.J. and Y.K. **Competing interests:** The authors declare that they have no competing interests.

**Data and materials availability:** All data needed to evaluate the conclusions in the paper are present in the paper and/or the Supplementary Materials.

Submitted 14 November 2023

Accepted 4 April 2024

Published 8 May 2024

10.1126/sciadv.adm9561